Radiative behavior of low-porosity ceramics: I-Development and applications of a physical optics modeling approach

Z.K. Low, D. Baillis

Version of Record: https://www.sciencedirect.com/science/article/pii/S0022407321003125
Manuscript_d965fe85b1e19265ef9cf184e7bff8f3

Radiative behavior of low-porosity ceramics: I– Development and applications of a physical optics modeling approach

Z.K. Low[a,b,*], D. Baillis[a]

[a] *Univ Lyon, INSA Lyon, CNRS, LaMCoS UMR5259, 69621 Villeurbanne, France.*
[b] *Saint-Gobain Research Provence, 84306 Cavaillon, France.*

Abstract

We propose a physical optics approach to compute the volume radiative properties and surface reflectivity of porous ceramics composed of a weakly absorbing solid matrix containing low fractions of heterogeneities (pores or particles). Our approach accounts for dependent scattering between heterogeneities that are small and close to each other compared to the wavelength, and only requires the 3D microstructure and complex refractive indexes of constituent phases as input. We performed numerical validation of our models on reference microstructures with known solutions, and showed that an accuracy of 5% is achieved. We then applied our approach to compute the spectral volume and surface radiative properties of tomography-reconstructed porous alumina samples of various porosities up to 30%. Microstructure-property relations are extracted from numerical results, and are compared to several analytical relations in order to assess their applicability in the studied material.

Keywords: Porous ceramics, Discrete dipole approximation (DDA), Radiative transfer equation (RTE), Volume radiative properties, Surface reflectivity

1. Introduction

Porous materials that combine attractive thermal and transport properties with good strength-to-weight ratio are found in many high-performance systems [1–3]: examples span a wide range of porosities and base materials, and include polymer foams used in building insulation [4], porous

*Corresponding author
Email address: zi.low@insa-lyon.fr (Z.K. Low)

Nomenclature

First- and second-order tensors ("vectors" and "matrices") are written in **bold face**.

Latin

A	Dipole interaction matrix
a	Radius
B	Blackbody radiance
C	Cross section
D	Target diameter
d	Cell size
E	Electric field
e	Basis vector
f	Volume fraction
g	Scattering asymmetry
h	Target height
I	Spectral radiance
j, k	Dipole indexes
k	Absorption index
ℓ	Chord length
L	Target length
M	Mueller matrix
m	Complex refractive index, $n + ik$
N	Number
n	Real refractive index; Normal vector
p	Parameter
P	Polarization
r	Distance
T	Temperature
u	Direction
v, w	Target replica indexes
V	Target volume
x	Position
y	Discretization parameter
$\mathbb{Z}$	Integer

Greek

α	Polarizability
Δ	Difference
ε	Permittivity
ϕ	Scattering phase function
κ	Absorption coefficient
λ	Wavelength
ρ	Reflectivity
σ	Scattering coefficient
τ	Transmissivity
θ	Angle
χ	Mie size parameter, $2\pi a/\lambda$
Ω	Solid angle

Superscripts and Subscripts

$'$	Modified quantity
0	Reference; *in vacuo*
abs	Absorption
amb	Ambient
diff	Diffuse
eff	Effective
ext	Extinction
Fr	Fresnel
h	Hemispherical
inc	Incident
m	Matrix
p	Pore/Particle
sca	Scattering
spec	Specular
sub	Substrate
tr	Transport

Operators and accents

∇	Del operator
$\cdot$	Dot product
$\langle\!\langle \bullet \rangle\!\rangle$	Stochastic mean
$\lvert\bullet\rvert$	Absolute value
$\hat{\bullet}$	Unit vector

Acronyms

DDA	Discrete dipole approximation
FCD	Filtered Coupled Dipole
FDTD	Finite-difference-time-domain
LDR	Lattice Dispersion Relation
RMS	Root-mean-squared
RTE	Radiative transfer equation

ceria particles for thermochemical reactions [5], and metal foams used in heat exchangers [6]. In particular, ceramics containing low fractions of pores, cracks and particles (see Figure 1) are often used at high temperatures where radiative transfer plays a major role [7, 8]. At the macroscopic length scales of interest, radiative transfer in such materials are usually described with the Radiative Transfer Equation (RTE) [1, 3], in which the influence of the micro-scale heterogeneities are represented by effective radiative properties. Accurate knowledge of the relation between the microstructure and the effective radiative properties is thus of paramount importance.

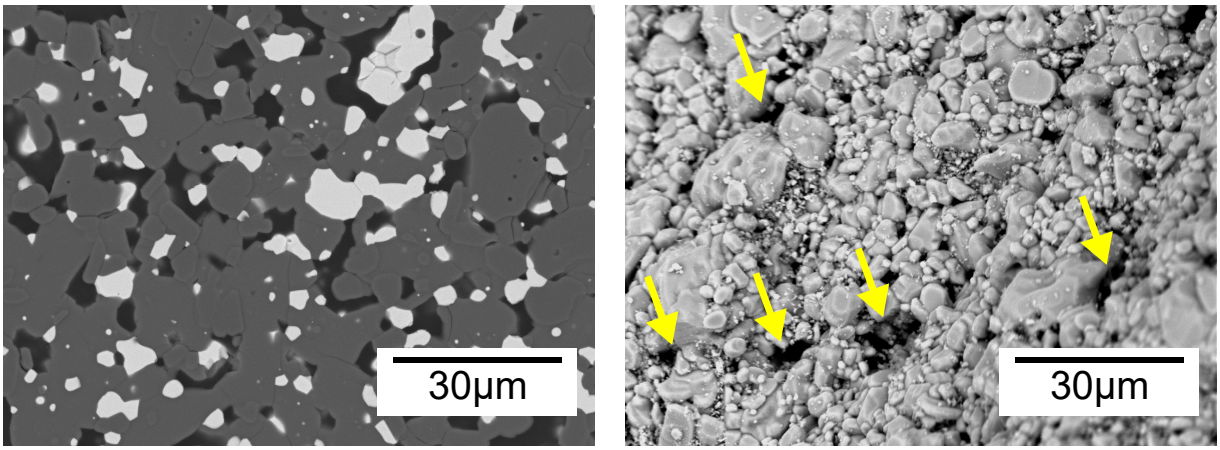

(a) Sectional view with pores (black) and particles (white). (b) Surface view with pores (indicated using arrows).

Figure 1: Scanning electron micrographs showing examples of porous ceramics.

While the effective radiative properties cannot be measured directly and have traditionally been identified from experimental data [2, 9], theoretical and numerical methods to predict these properties from the micro-scale morphology have seen significant progress. Past developments focused on both high-porosity materials (e.g., foams [4, 10], aerogels [11]) and semi-transparent solids with low pore and particle fractions [12, 13], since the dominant phase in both cases may be considered as the host medium for radiative transfer, and the secondary phases as absorbing and/or scattering heterogeneities. Purely theoretical predictions usually rely on known scattering and absorption properties of simple isolated geometries (e.g., spheres or infinite cylinders [14]), and invoke the independent scattering hypothesis [13] to calculate the effective properties of the material by summing the contributions of individual heterogeneities. This hypothesis usually fails when the volume fraction of heterogeneities exceed a few percent [15–20].

To model dependent scattering effects, Monte Carlo ray-tracing is a popular choice when characteristic length scales of the heterogeneities are larger than the wavelength, and has notably been performed on tomography-reconstructed or digitally generated porous ceramic microstructures [8, 10, 21–24]. However, when the heterogeneities are small and close to each other compared to the wavelength, resolution of Maxwell's equations via numerical methods [25] is necessary to account for wave effects, though the high computational cost generally limits the geometry sizes that can be simulated. The discrete dipole approximation (DDA) [26–28] has been used to compute the scattering and absorption properties by isolated particles or aggregates with complex geometry [5, 29, 30], which are often then used to deduce the effective radiative properties under the independent scattering framework [4, 11, 31–33]. Recently, a hybrid direct-inverse approach was proposed by Chen et al. [7] for 2D microstructures of zirconia ceramics with porosities of 5% to 20%: the angular distribution of scattered radiation is first simulated via the finite-difference-time-domain (FDTD) method, then used to identify the effective radiative properties by iteratively solving the RTE on an equivalent homogeneous medium. To our knowledge, direct physical optics methods to obtain the effective radiative properties of 3D microstructures while accounting for dependent scattering between small heterogeneities have not been implemented.

Note that most past work on low-porosity ceramics [8, 9, 13, 21, 22, 24, 34] assumed optically smooth material boundaries that reflect and refract specularly according to Fresnel's equations [3]. However, the presence of surface asperities generally lead to non-specular boundary scattering behavior [35, 36], with potential wave effects at wavelengths close to the asperity sizes. While analytical electromagnetic scattering solutions have been developed for Gaussian or exponential surfaces [35, 37, 38], numerical methods such as the FDTD with periodic boundary conditions have recently been applied to simulate the reflectivity of complex 3D microstructures [39, 40].

The present paper is the first part of a two-part study on the characterization of the infrared radiative behavior of low-porosity ceramics, outlined in Figure 2. In this paper, we propose a new approach to predict the volume radiative properties and surface reflectivity of materials composed of a weakly absorbing solid matrix and low volume fractions of pores or particles (around 20%). We determine the effective radiative properties from DDA simulations on tomography-reconstructed 3D microstructures, with the complex refractive indexes of the constituent phases as

input. This accounts for wave effects and dependent scattering when the pores and/or particles are small and close to one another compared to the wavelegnth. We perform numerical case studies on several reference microstructures to validate the choice of numerical parameters, then apply our method to simulate the volume and surface radiative properties of a porous alumina ceramic. We then compared our numerical results to several common analytical solutions in order to assess their applicability in the studied material. The determined effective radiative properties are applied in the second part of our study [41] to radiative transfer modeling of the reflectance, transmittance, and emittance of porous alumina disks. Comparison with experimental data obtained at temperatures up to 1300 °C allowed validation of the multi-scale numerical method.

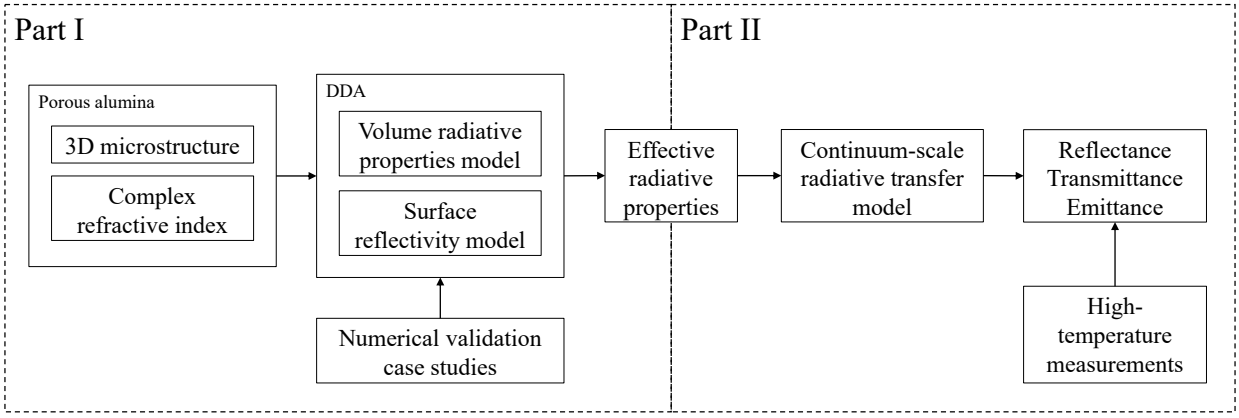

Figure 2: Outline of the two-part study.

Section 2 presents the radiative properties of interest and introduces two DDA-based models to compute these properties on volume elements on the material. Section 3 presents four case studies on reference microstructures with known solutions, and assesses the influence of key model parameters on the accuracy of the numerical results. Section 4 describes the acquisition and characterization of the 3D microstructure of the studied porous alumina ceramic, and compares the numerically and analytically predicted volume and surface radiative properties.

1.1. Mathematical notation

Tensor notation is used throughout this work, with first- and second-order tensors (commonly referred to as “vectors” and “matrices” respectively) denoted in bold characters. The spectral

dependence of energetic quantities and time dependence of electromagnetic fields are implied, and not denoted explicitly to improve readability.

2. Effective radiative properties modeling

We first recall the definitions of the effective volume and surface radiative properties of interest in section 2.1. We then propose a new physical optics approach to model these properties in section 2.2.

2.1. Definition of effective radiative properties

At the macro-scale, the heterogeneous material is modeled as an equivalent homogeneous semi-transparent medium, assumed isotropic with azimuthal asymmetry. The effective refractive index n_{eff} of the equivalent medium may be calculated analytically, for example with the volume-averaging definition [42]:

$$n_{\text{eff}}^2 = n_m^2 f_m + \sum_p n_p^2 f_p \tag{1}$$

where n is the refractive index and f is the volume fraction of the matrix (subscript m) and heterogeneities (subscript p for pores/particles) respectively.

The influence of the micro-scale heterogeneities on the macro-scale scattering and absorption behavior is represented through spectral effective properties, illustrated in Figure 3 and defined in this section. Note that the spectral dependence of all quantities is not denoted explicitly for readability.

Within the equivalent homogeneous medium, the spectral radiance I (radiance per unit vacuum wavelength) in an elementary solid angle $\mathrm{d}\Omega$ associated with the unit direction vector $\hat{\boldsymbol{u}}$ is modeled with the classic radiative transfer equation (RTE) [3]:

$$\hat{\boldsymbol{u}} \cdot \boldsymbol{\nabla} I(\hat{\boldsymbol{u}}) = -[\sigma_{\text{eff}} + \kappa_{\text{eff}}] I(\hat{\boldsymbol{u}}) + n_{\text{eff}}^2 \kappa_{\text{eff}} B(T) + \int_{4\pi} \sigma_{\text{eff}} \phi_{\text{eff}}(\hat{\boldsymbol{u}}', \hat{\boldsymbol{u}}) I(\hat{\boldsymbol{u}}') \, \mathrm{d}\Omega' \tag{2}$$

where σ_{eff} is the effective scattering coefficient, κ_{eff} is the effective absorption coefficient, and ϕ_{eff} is the effective scattering phase function, henceforth referred to as the effective volume radiative

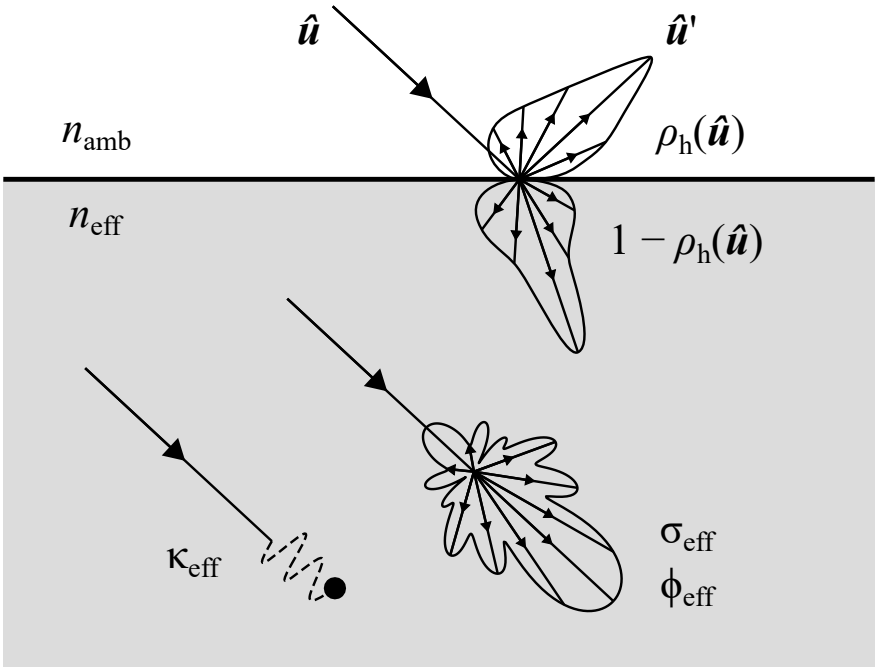

Figure 3: Schema of the equivalent homogeneous medium with its effective radiative properties.

properties. Note that ϕ_{eff} is normalized such that:

$$\int_{4\pi} \phi_{\text{eff}}(\hat{\boldsymbol{u}}, \hat{\boldsymbol{u}}')\, \mathrm{d}\Omega' = 1 \tag{3}$$

Since azimuthal symmetry is assumed, $\phi_{\text{eff}}(\hat{\boldsymbol{u}}, \hat{\boldsymbol{u}}') = \phi_{\text{eff}}(\theta)$ where θ is the angle between $\hat{\boldsymbol{u}}$ and $\hat{\boldsymbol{u}}'$.

We next assume that the heterogeneous material is placed in an ambient medium with refractive index $n_{\text{amb}} < n_{\text{eff}}$, separated by a sharp and non-absorbing boundary with outward-pointing unit normal vector $\hat{\boldsymbol{n}}$. Light incident on this boundary potentially undergoes complex interactions due to roughness effects [35]. In this work, we focus on the the reflective behavior of the material surface under illumination from the surrounding medium, represented by the bidirectional surface reflectivity $\rho(\hat{\boldsymbol{u}}, \hat{\boldsymbol{u}}')$ where $\hat{\boldsymbol{u}}$ and $\hat{\boldsymbol{u}}'$ are the directions of incident and scattered light respectively:

$$\rho(\hat{\boldsymbol{u}}, \hat{\boldsymbol{u}}') \equiv \frac{\int_{\Delta\Omega'} I_{\text{sca}}(\hat{\boldsymbol{u}}')\, \mathrm{d}\Omega' \left|\hat{\boldsymbol{u}}' \cdot \hat{\boldsymbol{n}}\right|}{\int_{\Delta\Omega} I_{\text{inc}}(\hat{\boldsymbol{u}})\, \mathrm{d}\Omega \left|\hat{\boldsymbol{u}} \cdot \hat{\boldsymbol{n}}\right|}, \quad \hat{\boldsymbol{u}} \cdot \hat{\boldsymbol{u}}' < 0 \tag{4}$$

where $\Delta\Omega$ is a small solid angle about the direction $\hat{\boldsymbol{u}}$. The directional-hemispherical surface

reflectivity under external illumination $\rho_{\mathrm{h}}(\hat{\boldsymbol{u}})$ is then calculated as follows:

$$\rho_{\mathrm{h}}(\hat{\boldsymbol{u}}) = \sum_{\hat{\boldsymbol{u}}\cdot\hat{\boldsymbol{u}}'<0} \rho(\hat{\boldsymbol{u}}, \hat{\boldsymbol{u}}') \tag{5}$$

2.2. Proposed physical optics approach

To take into account wave effects and dependent scattering within the porous ceramic, we propose a numerical approach that consists of solving Maxwell's equations on 3D microstructures using the Discrete Dipole Approximation (DDA) [26–28], then calculating the effective radiative properties from the DDA results. We first recall the key governing equations of the DDA (section 2.2.1), then describe our proposed model configurations to compute the volume and surface radiative properties (sections 2.2.2 and 2.2.3 respectively). We then end this section with an analysis on the main sources of uncertainty in our proposed approach (section 2.2.4).

2.2.1. Discrete dipole approximation (DDA)

The DDA, based on the volume integral form of the macroscopic Maxwell's equations, allows calculation of scattering and absorption by a dielectric object (henceforth referred to as the target) of arbitrary geometry [25, 26, 43, 44]. In this work, the formalism by Draine and Flatau [27, 28] is used. The DDA approximates the target as an array of N point dipoles on a regular cubic grid with cell size d. The ambient medium is considered transparent with refractive index n_{amb}. The complex refractive index $m_j = n_j + ik_j$ of each dipole is assumed isotropic in this work.

The target is illuminated by a monochromatic plane wave $\boldsymbol{E}_{\mathrm{inc}}$ of wavelength λ in the ambient medium, propagating in the direction $\hat{\boldsymbol{u}}$. Each dipole acquires a dipole moment $\boldsymbol{P}_j$ in response to the local electric field $\boldsymbol{E}_j$:

$$\boldsymbol{P}_j = \boldsymbol{\alpha}_j \cdot \boldsymbol{E}_j \tag{6}$$

where $\boldsymbol{\alpha}_j$ is the polarizability matrix of the dipole j, usually of the form $\boldsymbol{\alpha}(m_j, \lambda, d)$. The polarizability prescription is generally chosen on a case-by-case basis based on the problem studied (see the review by Yurkin et al. [45]). For our problems, we chose the Lattice Dispersion Relation [46] based on our sensitivity study in section 3.

Given $\boldsymbol{\alpha}_j$ of every dipole, Purcell and Pennypacker [26] showed that $\boldsymbol{P}_j$ may be obtained by

solving the following linear system of $3N$ complex equations:

$$\boldsymbol{E}_{\mathrm{inc},j} = \boldsymbol{\alpha}_j^{-1} \cdot \boldsymbol{P}_j + \sum_{k=1}^{N} \boldsymbol{A}_{jk} \cdot \boldsymbol{P}_k \tag{7}$$

where $\boldsymbol{A}_{jk}$ is a complex matrix describing the influence of the dipole k on the electric field at dipole j. Expressions of $\boldsymbol{A}_{jk}$ for isolated and periodic targets are given in references [27] and [28] respectively.

We resolved equation (7) in double precision using the open-source code DDSCAT (version 7.3.3, published on 10 July 2019 [27, 28, 47]), which solves for $\boldsymbol{P}$ iteratively with various complex conjugate gradient methods [48, 49]. As radiative heat transfer usually considers unpolarized light, DDA computations were performed for two orthogonal incident polarizations and the results were averaged. Key absorption and scattering characteristics such as cross-sections and Mueller matrix elements are then calculated from $\boldsymbol{P}$ in DDSCAT, as detailed in references [27, 28, 43, 47].

The next two subsections present our proposed configurations to compute the volume radiative properties (σ_{eff}, κ_{eff}, and ϕ_{eff}) and the bidirectional surface reflectivity $\rho(\hat{\boldsymbol{u}}, \hat{\boldsymbol{u}}')$ of porous ceramics.

2.2.2. Volume radiative properties

Inspired by the approach of Coquard and Baillis [50], we propose to calculate the effective volume radiative properties (scattering coefficient σ_{eff}, absorption coefficient κ_{eff}, and scattering phase function ϕ_{eff}) by considering the interaction of light with a spherical volume element of the material of diameter D, as illustrated in Figure 4.

The spherical target, composed of the matrix and pore/particle phases (with complex refractive indexes denoted $m_m = n_m + ik_m$ and $m_p = n_p + ik_p$ respectively), is illuminated by a monochromatic plane wave traveling in the direction $\hat{\boldsymbol{u}}$ in a non-absorbing surrounding medium for which we set the refractive index as $n_{\mathrm{amb}} = n_m$.

While we aim to model the extinction of light by scattering and absorption within the target volume, edge effects exist due to truncated pores/particles on the target boundary distorting the scattering behavior, and the mismatch between m_m and n_{amb} causing spurious reflections off the target boundary. To keep these edge effects to a minimum, we restrict our model to materials with

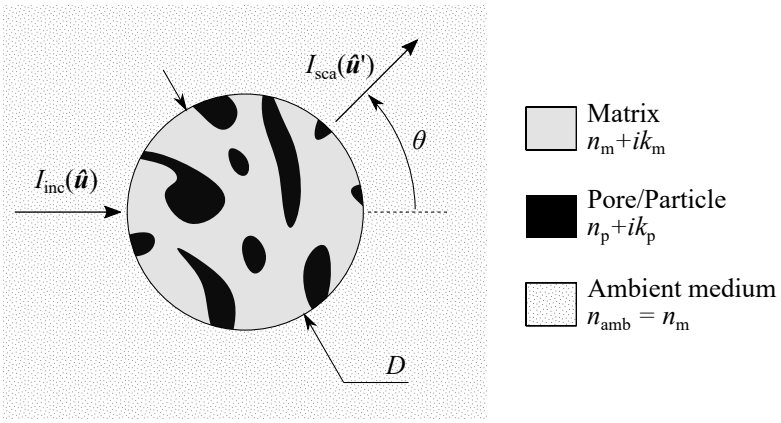

Figure 4: Computation of effective volume radiative properties from a spherical volume element of the material.

a weakly absorbing matrix phase (low k_m) having a significantly higher volume fraction than the pore/particle phases, and use targets much larger than the size of the heterogeneities as well as the wavelength of interest.

After calculating the scattering cross-section C_{sca}, absorption cross section C_{abs}, and first principal Mueller matrix element M_{11} of the spherical volume element via the DDA for isolated targets [27, 43], the effective volume radiative properties are then calculated as follows [50]:

$$\sigma_{eff} = \frac{C_{sca}}{V} \tag{8}$$

$$\kappa_{eff} = \frac{C_{abs}}{V} \tag{9}$$

$$\phi_{eff}(\theta) = \frac{M_{11}(\theta)}{\int_{4\pi} M_{11}(\theta)\,\mathrm{d}\Omega} \tag{10}$$

where V is the total volume of the spherical target (including pores, if any) and θ is the angle between $\hat{\boldsymbol{u}}$ and $\hat{\boldsymbol{u}}'$.

2.2.3. Bidirectional surface reflectivity

We consider that only heterogeneities from an optically thin region close to micro-scale rough surface contribute to macro-scale surface reflection. As such, we propose simulating a semi-infinite layer of thickness $h \ll 1/(\sigma_{eff}+\kappa_{eff})$ by applying periodic boundary conditions to a cuboidal volume element of the rough surface, illustrated in Figure 5a. The volume element is assumed aligned to the reference frame $\{\hat{\boldsymbol{e}}_1, \hat{\boldsymbol{e}}_2, \hat{\boldsymbol{e}}_3\}$ with $\hat{\boldsymbol{e}}_1$ perpendicular to the surface. The dimensions

of the volume element along the principal directions are denoted h, L_2, and L_3 respectively. The top surface is illuminated by a monochromatic plane wave traveling in the $\hat{\boldsymbol{u}}$ direction from the ambient medium of refractive index n_{amb}.

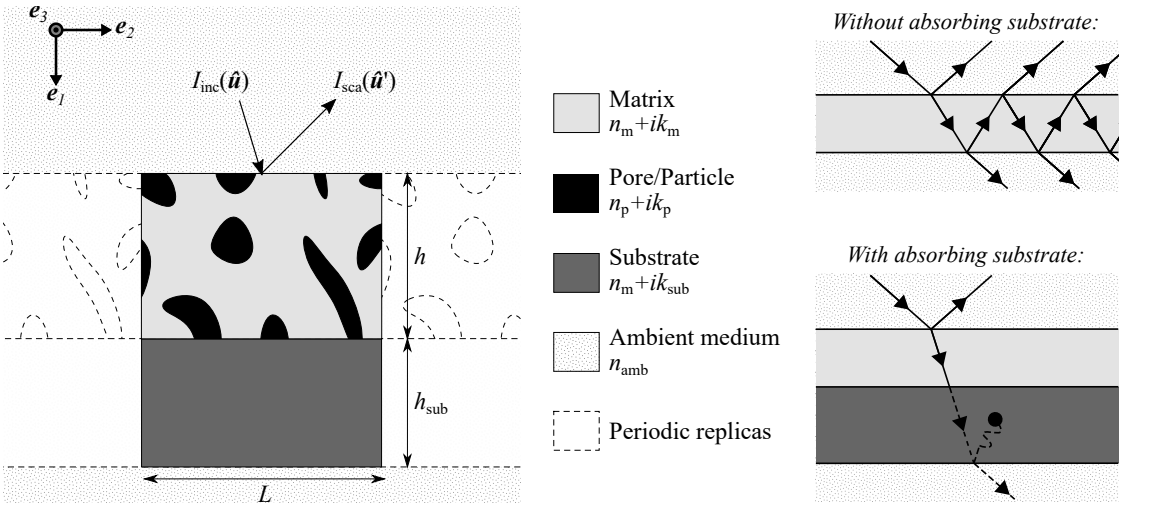

(a) Simulated configuration. (b) Role of the absorbing substrate.

Figure 5: Computation of the bidirectional interface reflectivity from a semi-infinite layer of the material atop an absorbing substrate, via application of periodic boundary conditions to a cuboidal volume element of the material.

A fraction of light entering the heterogeneous layer and reaching the bottom surface of the top layer is generally reflected upwards, which is undesirable as it leads to spurious multiple reflections as illustrated in Figure 5b for the case of a homogeneous top layer. To eliminate this phenomenon, we propose adding an absorbing substrate to the bottom of the heterogeneous layer. With appropriately chosen substrate properties (refractive index n_{sub}, thickness h_{sub}, and absorption index k_{sub}, see details in Appendix A), the interface between the top layer and the substrate becomes practically non-reflecting everywhere, save for the few locations where pores/particles are present. All light reaching the bottom surface of the top layer would then be transmitted into the substrate and absorbed.

For the proposed bilayered periodic volume element, DDSCAT calculates the so-called generalized Mueller matrix from which the bidirectional reflectivity $\rho(\hat{\boldsymbol{u}}, \hat{\boldsymbol{u}}')$ may be easily calculated (see Draine and Flatau [28]).

2.2.4. Uncertainty analysis

We identify and comment on the model parameters that represent the most important sources of uncertainty in the proposed approach. These parameters will be chosen and validated through convergence and sensitivity studies in section 3.

Uncertainty relating to cell size. In the DDA, the quantities and fields in the vicinity of each point dipole are assumed constant, which leads to discretization errors. Shape errors also arise from meshing non-cubic geometries with a regular cubic grid [45]. Both errors generally decrease with decreasing cell size d, though this leads to higher computational cost as N scales approximately with $d^{-}3$ [25, 27, 45].

In our present case, as we work with tomography-reconstructed microstructures, the input geometry has already been discretized into cubic voxels during the image acquisition process. Performing grid refinement by voxel subdivision (see illustration in Figure 6) thus reduces discretization errors only while maintaining the shape constant, which should improve grid convergence behavior.

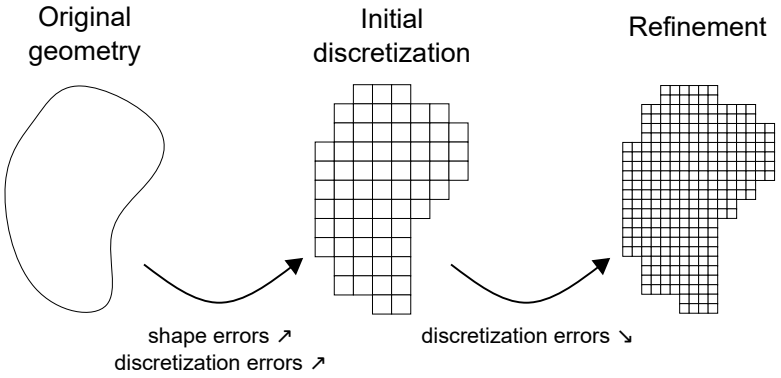

Figure 6: Shape and discretization errors in tomography-reconstructed geometries: true geometry, initial voxelization, and voxel refinement.

Past studies usually consider the discretization parameter y:

$$y = |m|d\frac{2\pi}{\lambda_0} \tag{11}$$

where $\lambda_0 = \lambda n_{\text{amb}}$ is the vacuum wavelength. Satisfactory results for the cross sections have been reported for $y < 1$ [27, 45], although $y < 0.5$ may be required if directional scattering quantities are

of interest [28]. We will determine appropriate values of y for our materials through convergence studies in section 3.

Uncertainty relating to polarizability model. The DDA requires the choice of a polarizability model $\boldsymbol{\alpha}$, which remains an open question: while early work used the well-known Clausius-Mosotti relation [26], many improvements have been proposed over the past few decades [44]. Performance of the different polarizabilities (in terms of grid convergence rate, accuracy at a given discretization, computational speed, etc.) depend on target geometry and refractive index [29] among other factors, and are usually assessed on a case-by-case basis through application on reference microstructures. We will justify our choice of prescription model through sensitivity studies in section 3.

Uncertainty relating to volume element size. For random microstructures, the volume element should be large enough to minimize edge effects, as well as ensure that the target microstructure and radiative behavior are truly representative of those of the material. Past work usually consider representative volume elements (RVEs) for which the simulated effective properties vary little from one sample to another [24, 51], thus allowing determination of the effective properties of the continuum with good precision from a single RVE.

However, it has been shown [52, 53] that the RVE size can be prohibitively large in random porous media, and that statistical effective properties may instead be deduced from computations on a large number of smaller, non-representative volume elements. This is exacerbated in the present approach by the computationally demanding nature of the DDA. We show in sections 3.1.2, 4.2 and 4.3 that while the RVE is never attained in the present case, microstructure-property relations may still be deduced from numerical results with good accuracy.

3. Numerical validation case studies

In this section, we simulate the radiative characteristics of reference microstructures with known solutions, and study the influence of several model parameters (previously discussed in section 2.2.4) on the accuracy of our results. This serves to demonstrate and numerically validate our proposed modeling approach before it is applied to the study of a real material in section 4.

For each type of model, two reference microstructures of comparable composition and complexity to porous multiphase ceramics are considered:

1. Volume radiative properties modeling on isolated spherical volume elements;
    - Scattering and absorption by a multilayered sphere with an absorbing matrix phase (section 3.1.1);
    - Scattering coefficient of a transparent solid containing random monodisperse non-overlapping spherical pores (section 3.1.2);
2. Reflectivity modeling using periodic boundary conditions on cuboidal volume elements;
    - Reflectance of a periodic ordered opal structure (section 3.2.1);
    - Specular interface reflectivity of a homogeneous semi-infinite surface (section 3.2.2).

The influence of cell size d and volume element size V are assessed through convergence studies on these microstructures. For the polarizability α, we compared two prescriptions that we deemed the most appropriate based on the review by Yurkin and Hoekstra [44]: the Lattice Dispersion Relation (LDR) by Gutkowicz-Krusin and Draine [46] and the Filtered Coupled Dipole (FCD) prescription by Piller and Martin [54].

3.1. Volume radiative properties modeling

3.1.1. Multilayered sphere with an absorbing matrix phase

We first consider the scattering and absorption behavior of a multilayered sphere for which exact solutions can be obtained with Mie theory [14, 55]. Figure 7a illustrates the radii and composition of the different layers, chosen such that the solid matrix phase m has a volume fraction of $f_m \approx 0.70$, while the pore (1) and particle (2) phases have fractions $f_1 \approx 0.18$ and $f_2 \approx 0.12$ respectively. The complex refractive indexes m of the three phases at selected wavelengths are given in Table 1. The refractive index of the ambient medium is set to $n_{\text{amb}} = n_m$ following the configuration defined in section 2.2.2.

As discussed in section 2.2.4, shape errors in tomography-reconstructed geometries are usually introduced during image acquisition only, and further voxel refinement only reduces the discretization errors. These errors are studied separately through two discretization techniques:

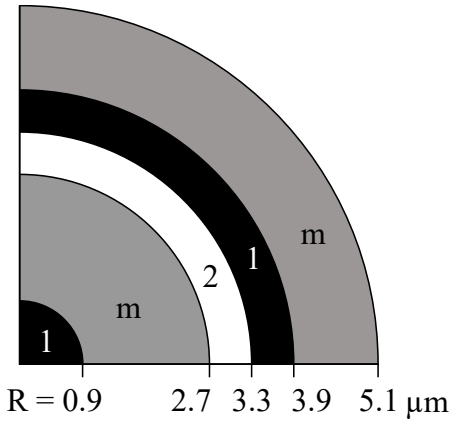

(a) Radii and composition.

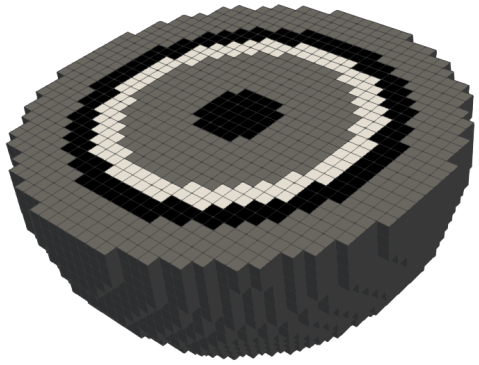

(b) Rough initial discretization with cell size $d_0 = 300\,\text{nm}$.

Figure 7: Schema of the multilayered sphere. The matrix phase (m) is represented in gray, while the pore (1) and particle (2) phases are represented in black and white respectively.

λ_0 (µm)	$m_m = n_m + k_m i$	$m_1 = n_1$	$m_2 = n_2 + k_2 i$
1	$1.645 + 6.880 \times 10^{-7} i$	1.000	$2.079 + 1.428 \times 10^{-6} i$
2	$1.632 + 1.239 \times 10^{-6} i$	1.000	$2.068 + 1.208 \times 10^{-6} i$
3	$1.611 + 1.613 \times 10^{-6} i$	1.000	$2.048 + 1.092 \times 10^{-6} i$
4	$1.578 + 1.201 \times 10^{-5} i$	1.000	$2.020 + 4.538 \times 10^{-6} i$
5	$1.534 + 2.017 \times 10^{-4} i$	1.000	$1.982 + 7.110 \times 10^{-5} i$
6	$1.473 + 1.340 \times 10^{-3} i$	1.000	$1.933 + 5.458 \times 10^{-4} i$
7	$1.392 + 6.907 \times 10^{-3} i$	1.000	$1.870 + 2.489 \times 10^{-3} i$
8	$1.291 + 2.259 \times 10^{-2} i$	1.000	$1.800 + 1.016 \times 10^{-2} i$
9	$1.161 + 3.529 \times 10^{-2} i$	1.000	$1.707 + 6.246 \times 10^{-3} i$
10	$0.961 + 5.397 \times 10^{-2} i$	1.000	$1.581 + 8.728 \times 10^{-3} i$

Table 1: Complex refractive indexes m for the matrix (m), pore (1) and particle (2) phases of the multilayered sphere at selected vacuum wavelengths λ_0.

- A "roughly discretized sphere" (see sectional view in Figure 7b) obtained by first applying an initial discretization of $d_0 = 300\,\text{nm}$ to the multilayered sphere , then subdividing each voxel as many times as necessary to obtain the desired final cell sizes d. This keeps the initial shape constant, allowing the study of discretization errors independently of shape errors. Three final cell sizes were considered: $d = 75\,\text{nm}$, 60 nm, and 50 nm, corresponding to maximal discretization parameters y of 0.98, 0.78, and 0.65 respectively at $\lambda_0 = 1\,\mu\text{m}$.

- A "finely discretized sphere" obtained by applying a fine initial discretization without further refinement ($d_0 = d = 50\,\text{nm}$). This allows the study of shape errors in addition to

discretization errors.

Figure 8 shows the reference scattering and absorption cross sections from Mie theory, and the errors in the DDA results obtained on the roughly discretized sphere using different polarizabilities and cell sizes. For vacuum wavelengths below 4 µm, relative errors in the scattering cross section are generally low, indicating a limited influence of shape errors. On this wavelength range, the LDR generally gives equal or lower errors than the FCD, with results that are practically independent of cell size. On the other hand, high relative errors in the absorption cross section are observed on this range, but they are merely a consequence of the extremely low absorption, and are thus of little concern.

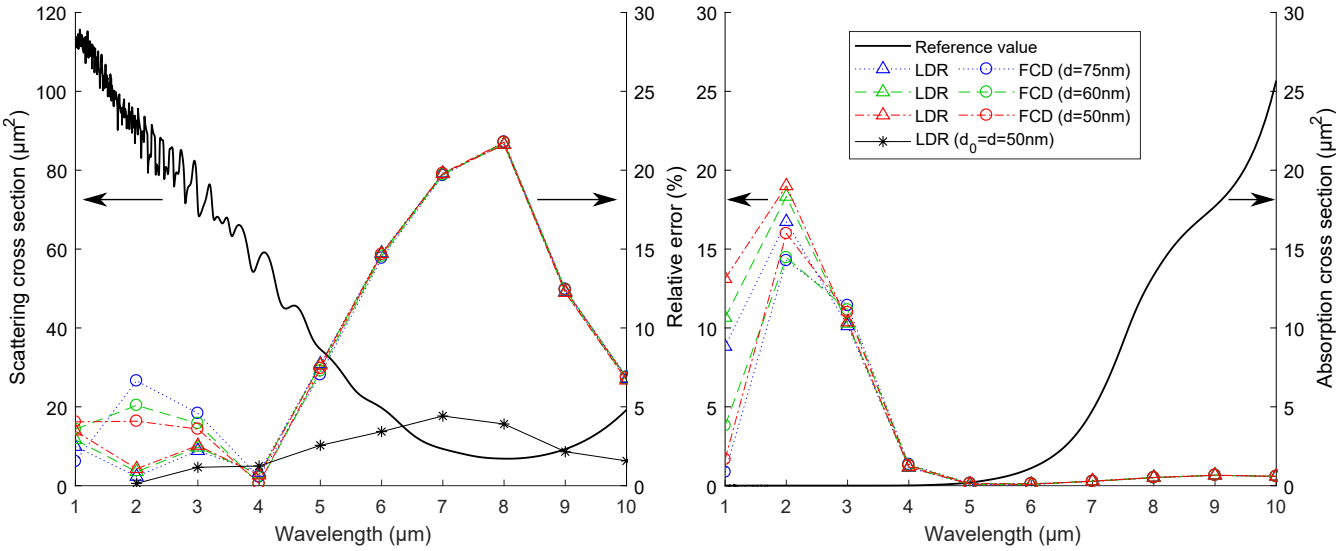

Figure 8: Scattering (left) and absorption (right) cross sections of a multilayered sphere: reference Mie solution (thick black lines) and errors in DDA results obtained on a roughly discretized sphere of initial cell size $d_0 = 300\,\text{nm}$, using the Lattice Dispersion Relation [46] (LDR, △) and Filtered Coupled Dipole [54] (FCD, ○) polarizabilities. Results are shown for three final cell sizes: $d = 75\,\text{nm}$ (dotted lines), $d = 60\,\text{nm}$ (dashed lines), and $d = 50\,\text{nm}$ (dash-dot lines). For the scattering cross section, additional results obtained with a finer initial discretization of $d_0 = d = 50\,\text{nm}$ are also given (∗ connected with thin lines).

At vacuum wavelengths of 4 µm and higher, DDA results obtained on the roughly discretized sphere are essentially independent of polarizability and cell size. The absorption cross section shows excellent agreement with the Mie solution. However, the scattering cross section differed by as high as 22% due to shape errors. Indeed, with the finely discretized sphere ($d_0 = d = 50\,\text{nm}$), the discrepancy in the scattering cross section becomes lower than 5% on the whole wavelength

range. Similar conclusions can be drawn from Figure 9, in which the Mueller matrix element M_{11} at $\lambda_0 = 2\,\mu\text{m}$ obtained with the LDR are compared to the Mie solution. The results on the roughly discretized sphere appear insensitive to cell size, with discrepancies practically disappearing with the finely discretized sphere, indicating a strong influence of shape errors especially on backwards scattering.

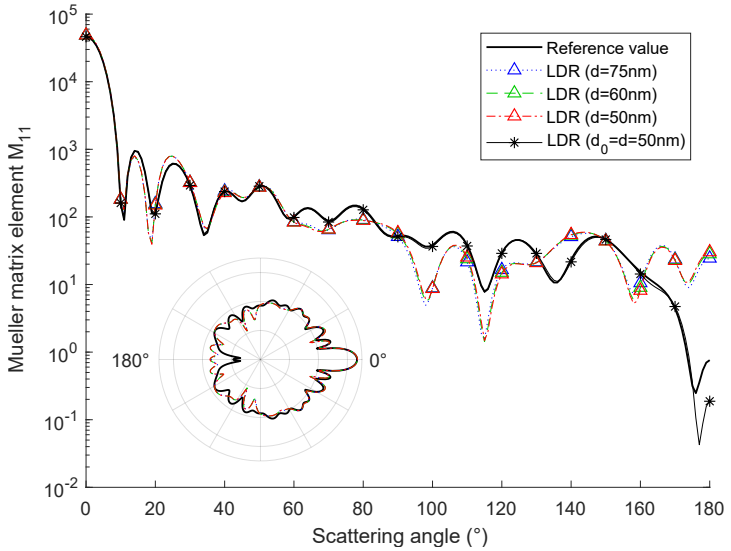

Figure 9: Mueller matrix element M_{11} of a multilayered sphere at a vacuum wavelength of $\lambda_0 = 2\,\mu\text{m}$: reference Mie solution (thick black line) and DDA results obtained on a roughly discretized sphere of initial cell size $d_0 = 300\,\text{nm}$ using the Lattice Dispersion Relation [46] (LDR, △) polarizability. Results are shown for three final cell sizes: $d = 75\,\text{nm}$ (dotted lines), $d = 60\,\text{nm}$ (dashed lines), and $d = 50\,\text{nm}$ (dash-dot lines). In addition, results obtained with a finer initial discretization of $d_0 = d = 50\,\text{nm}$ are also given ($*$ connected with thin lines). Note that the angle 0° corresponds to forward scattering and 180° to backward scattering, and that scattering patterns are plotted on a logarithmic scale, both in the main graph and the inset.

From our results, we conclude that the accuracy of DDA modeling on non-cuboidal geometries is mainly influenced by shape errors rather than discretization errors, highlighting the importance of a fine initial discretization (or imaging resolution in the case of tomography-reconstructed geometries). For such geometries, using the LDR polarizability model at $y \leq 0.81$ should provide numerical results accurate to within 5%.

3.1.2. Transparent solid with random spherical pores

We next simulate the volume radiative properties at $\lambda_0 = 1\,\mu\text{m}$ of a transparent solid matrix ($n_m = 1.718 = n_{\text{amb}}$) containing monodisperse non-overlapping spherical pores ($n_p = 1$) of radius

$a_p = 0.9\,\mu\text{m}$, equivalent to a Mie size parameter of $\chi_p = 2\pi a_p/\lambda = 9.71$. The base microstructure of nominal porosity $f_p = 0.08$ is generated through random sequential adsorption. The scattering coefficient of the material is then computed from spherical subvolumes of the base microstructure according to the method presented in section 2.2.2. The LDR [46] polarizability prescription and a discretization of $d = 75\,\text{nm}$ ($y = 0.81$) were chosen based on the conclusions of the previous validation study.

As discussed in section 2.2.4, due to memory constraints, it is impossible to perform DDA calculations on a single volume element large enough to be considered a RVE while maintaining a sufficiently fine discretization. We aim to demonstrate here that it is possible to estimate the statistical effective properties of the material from a large number of smaller, non-representative volume elements, without recourse to classic RVE-based approaches [24, 51].

We considered volume elements with diameters ranging from $D = 6.6\,\mu\text{m}$ to $D = 13.5\,\mu\text{m}$. For each volume element size, between 27 and 125 samples were extracted from the base microstructure. On the left of Figure 10, the scattering coefficient of each volume element is plotted as a function of its porosity and diameter. As expected, the porosity and scattering coefficient vary significantly between volume elements of the same diameter D due to the sub-RVE sizes considered.

Nonetheless, we observe that the relation between the porosity and the computed scattering coefficient is quasi-linear, and converges well with increasing volume element size D. The plot on the right of Figure 10 shows the evolution of the scattering coefficient at the nominal porosity $f_p = 0.08$, evaluated through linear laws fitted our to numerical results, for $D \geq 10.2\,\mu\text{m}$. The uncertainty arising from microstructural variability, estimated from the root-mean-squared (RMS) error of the linear regression and represented by error bars, also stabilizes at ±5% beyond that threshold.

We also compared our results in Figure 10 to the independent scattering solution (equation (12)):

$$\sigma_{\text{eff}} = C_{\text{sca}}^{\text{Mie}}(n_m, \chi_p)\frac{f_p}{\frac{4}{3}\pi a_p^3} \tag{12}$$

where $C_{\text{sca}}^{\text{Mie}}$ is the scattering cross section of a single pore given by Mie theory [14, 55]. Discrep-

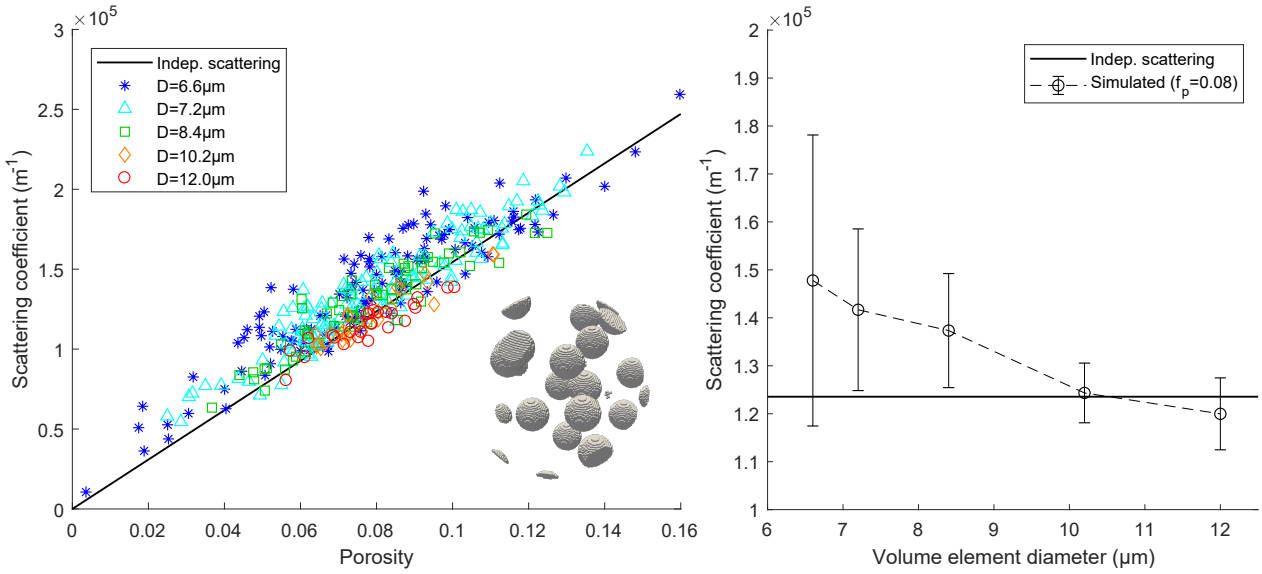

Figure 10: Scattering coefficient at $\lambda_0 = 1\,\mu\text{m}$ computed from spherical volume elements containing a transparent solid matrix with monodisperse non-overlapping spherical pores. (a) Simulated results as a function of porosity. Each point represents DDA results for a single volume element of diameter D. The independent scattering solution (black line) is also given. An example target with $D = 10.2\,\mu\text{m}$ is featured in the inset, with only the pores shown. (b) Convergence of simulated scattering coefficient at $f_p = 0.08$ with D (points), compared to the independent scattering solution (line).

ancies between our numerical results and the independent scattering solution are mainly due to edge effects (notably the presence of truncated pores at the boundary), which generally diminish with increasing D. The presence of pores close to each other within the volume element may also contribute to discrepancies; nevertheless, as the mean distance between pores [56] is large (about $7\,\mu\text{m} \approx 12\lambda$), our converged numerical results remain close to the independent scattering solution [20].

Our results show that despite the sub-RVE sizes of the volume elements considered, converged microstructure-property relations may still be deduced from computations on a large number of sufficiently large volume elements. For example, in the present case study, convergence is considered to be achieved at $D = 10.2\,\mu\text{m}$. Appropriate statistics, such as the RMS error of the regression, allow estimation of the uncertainty due to microstructural variability. The post-processing strategy demonstrated in this case study will be applied in section 4.2 to the case of the tomography-reconstructed porous alumina sample.

3.2. Reflectivity modeling

3.2.1. Periodic ordered opal structure

We next simulate the normal-hemispherical reflectance of a semi-infinite ordered opal structure. The periodic unit cell, composed of alumina spheres 1 μm in diameter arranged in a hexagonal close packed lattice such that the porosity is $f_p = 0.24$ (see Figure 11), has been described by Liu et al. [39] who also provided reference results via finite-difference-time-domain (FDTD) computations. Note that unlike the FDTD method which requires the simulation of a 2×2 tessellation of unit cells for convergence [39], in DDA computations [28], only one unit cell needs to be simulated.

We first perform a grid convergence study by applying different levels of initial discretization without further refinement ($d = d_0$). In addition, we also compared two polarizability prescriptions (LDR [46] and FCD [54]). Results for selected wavelengths are plotted as a function of discretization parameter y in Figure 11a. We observe a smooth grid convergence behavior for wavelengths of $\lambda_0 = 1.5\,\mu\text{m}$ and above, while for shorter wavelengths, a much higher sensitivity to cell size and polarizability is observed. A low discretization parameter y of between 0.15 and 0.09 depending on wavelength is required for grid convergence, of the same order as grid sizes used by Liu et al. [39]. Note that this is much stricter than the $y < 0.5$ criterion that Draine and Flatau [28] proposed for DDA simulations on homogeneous thin slabs, likely due to the more complex microstructure in the present case. Converged results for both the LDR and FCD polarizabilities are practically identical.

We also compared results obtained with $d = 12.5\,\text{nm}$ (i.e., $y \leq 0.18$ with the maximum at $\lambda_0 = 0.76\,\mu\text{m}$) to reference results by Liu et al. [39] in Figure 11b. Excellent agreement is found, especially on the wavelength range $\lambda_0 \geq 1.5\,\mu\text{m}$ where the reflectance varies smoothly with wavelength. At $\lambda_0 < 1.5\,\mu\text{m}$, sharp peaks and dips in the reflectance are observed and are due to resonance effects from the highly ordered microstructure. Shape errors due to discretization can thus have a large impact on this wavelength range, which explains the discrepancies at certain resonance peaks between our results and the reference as well as the slow grid convergence.

We thus conclude that for both the LDR and FCD polarizabilities, the DDA gives accurate results for the reflectance of the ordered opal structure with a discretization of $y \approx 0.15$ for wave-

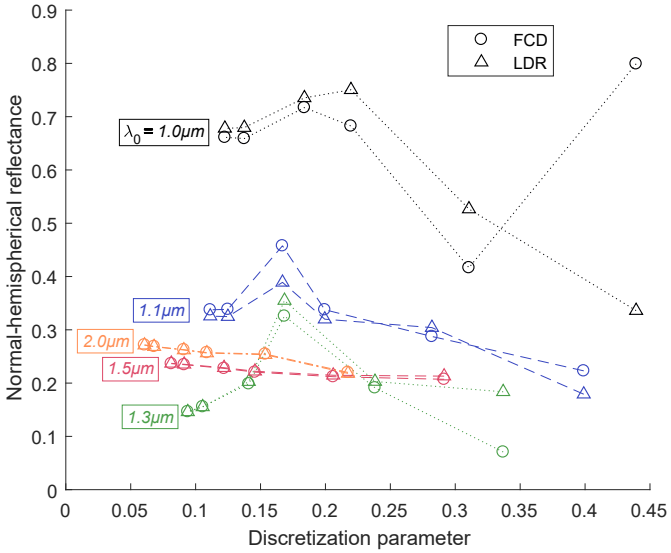

(a) Grid convergence results for selected wavelengths.

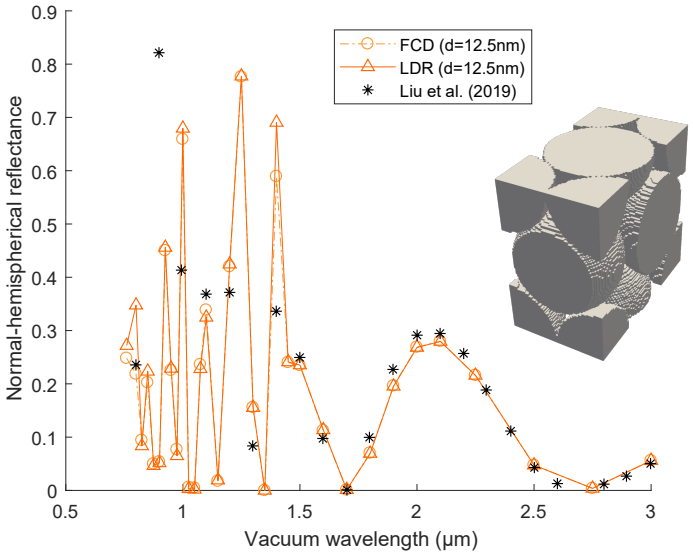

(b) Comparison with results by Liu et al. [39].

Figure 11: Spectral normal-hemispherical reflectance of an ordered opal structure [39] simulated with the DDA with the Lattice Dispersion Relation [46] (LDR, △) and Filtered Coupled Dipole [54] (FCD, ○) polarizability prescriptions. Converged results obtained with $d = 12.5\,\text{nm}$ are compared to reference results by Liu et al. [39] (∗), with the corresponding periodic unit cell illustrated in the inset.

lengths above 1.5 μm, although a much finer grid ($y \leq 0.09$) may be needed for grid convergence at shorter wavelengths due to resonance effects. Note however that the extreme sensitivity to shape errors is a particularity of the ordered opal structure where resonance effects dominate at certain

wavelengths, and should be less of a problem for tomography-reconstructed random porous ceramics.

3.2.2. *Homogeneous semi-infinite surface*

Our final case study aims to assess the accuracy of the surface reflectivity computed according to the method proposed in section 2.2.3. Recall that this involves simulating a semi-infinite top layer representing the studied surface, sitting atop an absorbing substrate with appropriately chosen properties to simulate non-reflecting boundary conditions (see Appendix A). We consider the case of a smooth, homogeneous, and transparent top layer of refractive index $n_m = 1.718$ surrounded by vacuum ($n_{\text{amb}} = 1$), illuminated at normal incidence. The model should thus predict the normal interface reflectivity given by Fresnel's equations [3, 57]:

$$\rho_{\text{h}}(\hat{\boldsymbol{u}}) = \rho_{\text{Fr}}(\hat{\boldsymbol{u}}) = \left(\frac{n_m - n_{\text{amb}}}{n_m + n_{\text{amb}}}\right)^2 \tag{13}$$

We performed a grid convergence study for different top layer thicknesses h, using the LDR [46] and FCD [54] polarizabilities. Results are shown in Figure 12. The variation of reflectivity with the discretization parameter y is well-described by a second-order polynomial as observed by Yurkin et al. [45], thanks to the absence of shape errors. The FCD gives higher errors at equal cell sizes compared to the LCD, and the results are also more sensitive to cell size.

We observe that using the LDR polarizability with a discretization of $y < 0.4$ is sufficient to give results within 5% of the target value, regardless of the top layer thickness h. It should be noted that due to slight imperfections in the proposed implementation of non-reflecting boundary conditions (see Figure A.18b), a small discrepancy of about ±2.5% may persist even with much smaller discretizations.

3.3. *Summary of validation studies*

Through convergence and sensitivity studies in this section on reference geometries, we were able to establish guidelines for the choice of model parameters, namely the polarizability α, cell size d, and volume element size V. The accuracy of our models were also estimated. Key takeaways are summarized below:

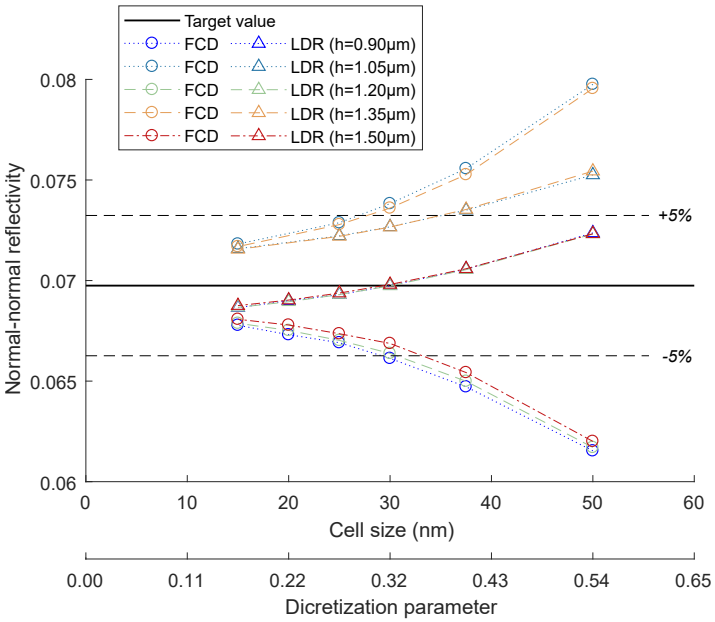

Figure 12: Normal-normal reflectivity of a homogeneous semi-infinite surface simulated from a thin layer of thickness h atop an absorbing substrate: DDA grid convergence results for different h and polarizability prescriptions (Lattice Dispersion Relation, LDR [46] and Filtered Coupled Dipole, FCD [54]), compared to the target reflectivity from Fresnel's equations [3] with a ±5% error band.

- The influence of shape errors was shown in section 3.1.1 to be non-negligible when simulating non-cubic shapes. For to tomography-reconstructed microstructures, the resolution during the imaging process should thus be as fine as possible. Further grid refinement is then performed by voxel subdivision.

- Complete grid independence required extremely fine discretizations (e.g. $y < 0.09$ for the ordered opal structure in section 3.2.1) regardless of polarizability model. However, this level of discretization is impractical as it severely limits the volume element sizes that can be simulated.

- Using the Lattice Dispersion Relation (LDR [46]) polarizability, numerical results accurate to within 5% of reference solutions were obtained with a discretization of $y < 0.81$ for the computation of volume radiative properties, and $y < 0.4$ for reflectivity simulations.

- The Filtered Coupled Dipole (FCD [54]) polarizability generally gave less accurate results for the studied materials and microstructures at constant cell size.

- DDA computations on representative volume elements (RVE) of random materials are usually prohibitively expensive. Nevertheless, our results in section 3.1.2 show that convergence of the statistical radiative properties may still be achieved through computations on a large number of volume elements smaller than the RVE.

4. Application to a porous alumina ceramic

We now apply our numerically validated models to compute the room-temperature effective radiative properties of a tomography-reconstructed porous α-alumina ceramic for selected wavelengths between $\lambda_0 = 1\,\mu\text{m}$ and $\lambda_0 = 7\,\mu\text{m}$. The material and its microstructure are first described in section 4.1. Results of volume radiative properties modeling and surface radiative properties modeling are then presented and discussed in sections 4.2 and 4.3 respectively.

4.1. Material and microstructure

The studied material is a high-purity porous sintered alumina ceramic, composed of 99% α-alumina by mass. The median grain diameter is 2.9 µm before sintering. Judging by the high purity and large grain sizes, grain boundary scattering may be neglected [58]. As such, the solid matrix is modeled as isotropic and homogeneous, and its refractive index n_m and absorption index k_m are calculated by applying the averaging relation of Pajdzik and Glazer [59] to room-temperature optical measurements on birefringent alumina monocrystals [60]. Table 2 lists n_m and k_m for the wavelengths λ_0 of interest. The pore phase is composed of air ($n_p = 1$ and $k_p = 0$).

λ_0 (µm)	n_m	k_m
1.0	1.718	1.362×10^{-41}
1.5	1.712	8.119×10^{-21}
2.0	1.704	7.223×10^{-14}
3.0	1.680	4.251×10^{-9}
4.0	1.644	3.434×10^{-7}
5.0	1.594	2.775×10^{-5}
6.0	1.527	2.375×10^{-4}
7.0	1.435	1.942×10^{-3}

Table 2: Refractive index n_m and absorption index k_m of the polycrystalline alumina matrix at 295 K at selected vacuum wavelengths λ_0.

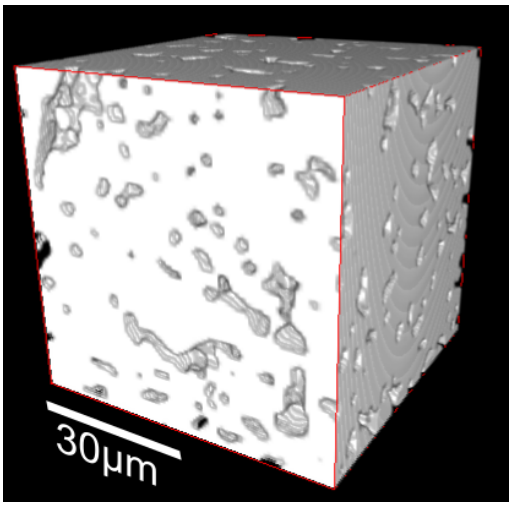

Figure 13: Tomography-reconstructed porous alumina ceramic with physical dimensions of 60 µm × 60 µm × 60 µm and a resolution of 0.3 µm per voxel. The alumina phase is in white while the voids are the air-filled pores.

X-ray tomography (RX Solutions EasyTom Nano) was performed on a small ceramic sample at the MATEIS laboratory (Villeurbanne, France). Image processing with the Fiji software [61] provided a 60 µm × 60 µm × 60 µm 3D binary reconstruction of the material with a voxel size of $d_0 = 0.3\,\mu\text{m}$, shown in Figure 13. The nominal porosity of the ceramic is $f_p = 0.12$, determined from the volume fraction of the void phase voxels. The characteristic pore size was estimated through the pore phase mean chord length [56] as $\langle\langle \ell_p \rangle\rangle = 1.8\,\mu\text{m}$.

The low values of k_m and f_p in the studied porous ceramic agree with the hypotheses behind our proposed approach in section 2.2. The material data in Table 2 and the image in Figure 13 was used as input data for the numerical models. The tomography-reconstructed microstructure is converted into a dipole array by placing one dipole at the center of each voxel, eventually after one or more voxel subdivisions (see Figure 6) to ensure a sufficiently fine discretization.

4.2. Results of volume radiative properties modeling

We compute the volume radiative properties for the wavelengths listed in Table 2 according to the method described in section 2.2.2. We used the LDR [46] polarizability with a discretization parameter of $y < 0.81$, which our convergence studies in section 3.1.1 suggested would give results accurate to within 5%. This required cell sizes of $d = 75\,\text{nm}$ for $\lambda_0 < 2\,\mu\text{m}$, $d = 150\,\text{nm}$ for $2\,\mu\text{m} \leq \lambda_0 < 4\,\mu\text{m}$, and $d = d_0 = 300\,\text{nm}$ for $\lambda_0 \geq 4\,\mu\text{m}$.

DDA computations were performed on non-overlapping spherical volume elements of equal diameter D sampled from the reconstructed microstructure. The values of D were chosen to fulfill the criteria $D > \langle\langle \ell_p \rangle\rangle$ and $D > \lambda_0$. To keep computational demands within reasonable limits, we also limited the volume element size to $D \leq 200d$ ($N \leq 4.2$ million dipoles, requiring ≤ 20 CPU-hours of iterative resolution). The number of volume elements range from 1 to 125 depending on the chosen value of D. The porosity f_p and mean pore phase chord length $\langle\langle \ell_p \rangle\rangle$ [56] of each volume element are also computed.

Per the strategy outlined in section 3.1.2, numerical results are compared to the predictions of several analytical models, and used to extract microstructure-property relations.

4.2.1. Effective absorption coefficient

Figure 14 shows the effective absorption coefficient κ_{eff} computed with the DDA for wavelengths $\lambda_0 = 6\,\mu\text{m}$ and $7\,\mu\text{m}$. Results for volume elements of different diameters D are compared, with the number of non-overlapping samples ranging from 64 at the smallest diameter to 1 for $D > 30\,\mu\text{m}$.

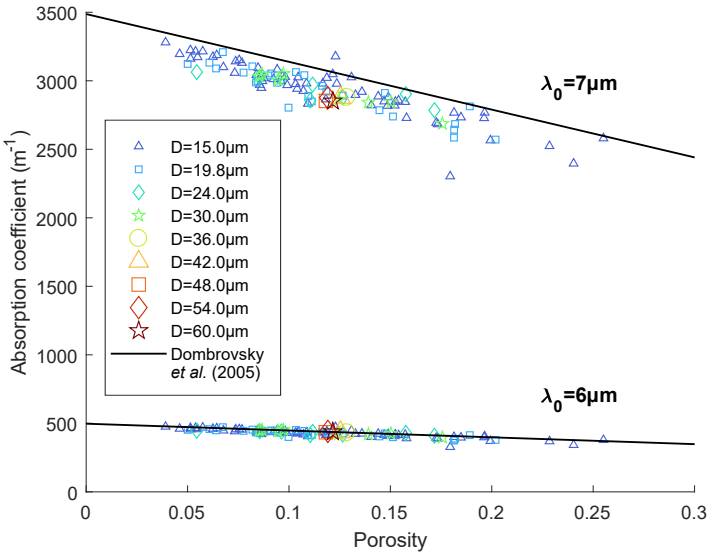

Figure 14: Effective absorption coefficient as a function of porosity computed with the DDA on volume elements of different diameters D (shown as different symbols) for wavelengths $\lambda_0 = 6\,\mu\text{m}$ and $7\,\mu\text{m}$, compared to the analytical relation for matrix absorption proposed by Dombrovsky et al. [12] (equation (14), thick lines).

We also compare the results to equation (14), initially proposed by Dombrovsky et al. [2, 12]

for porous ceramics with low solid phase absorptivity :

$$\kappa_{\text{eff}} = \frac{4\pi k_m}{\lambda_0} f_m \tag{14}$$

For $\lambda_0 = 6\,\mu\text{m}$ at which $k_m = 2.375 \times 10^{-4}$, an excellent agreement between the numerical DDA results and the model of Dombrovsky et al. [12] is observed regardless of the volume element size D, with a RMS deviation between the analytical and numerical results of 4.5% at $D = 15\,\mu\text{m}$ (64 samples) and 1.8% at $D = 30\,\mu\text{m}$ (8 samples). Equally good results were also observed for smaller wavelengths at which k_m are several orders of magnitude lower; they are not represented in Figure 14 to preserve legibility.

On the other hand, for $\lambda_0 = 7\,\mu\text{m}$ at which $k_m = 1.942 \times 10^{-3}$, the analytical model very slightly overestimates κ_{eff}. This is because scattering by heterogeneities modify the path lengths traveled by light in the matrix and thus the amount of light absorbed, which is neglected by the model of Dombrovsky et al. [12] leading to deviations at high enough matrix absorptivities. These deviations remain very small in the present material and wavelength, with a RMS value of 5.0% over 8 samples of $D = 30\,\mu\text{m}$ and 6.9% for the single $D = 60\,\mu\text{m}$ sample. We thus consider the use of the model of Dombrovsky et al. [12] justified for the considered wavelengths.

While wavelengths greater than $\lambda_0 = 7\,\mu\text{m}$ are beyond the scope of this study, we note that the accuracy of this analytical model is expected to further degrade on this range, since the absorptivity of alumina increases while approaching the Christiansen wavelength ($\approx 10\,\mu\text{m}$) at which it exhibits blackbody-like behavior [60].

4.2.2. Effective scattering coefficient and phase function

Figure 15 shows, on the left, the variation of effective scattering coefficient σ_{eff} with porosity computed with the DDA on volume elements of different sizes D, and on the right, the scattering phase function ϕ_{eff} for different values of D averaged over volume elements of porosity $f_p = 0.12 \pm 0.01$. Results at wavelengths $\lambda_0 = 2\,\mu\text{m}$ and $\lambda_0 = 7\,\mu\text{m}$ are given. The number of non-overlapping samples ranging from 125 at the smallest diameter to 1 for $D > 30\,\mu\text{m}$.

The independent scattering solution for monodisperse spherical pores (equation (12)) is also

given with the pore radius estimated from the nominal mean chord length:$a_p = 0.75\langle\langle \ell_p \rangle\rangle = 1.38\,\mu\text{m}$ [62]. The influence of a variation of ±17% in a_p, reflecting the uncertainty in the mean chord length, is also shown.

For the scattering coefficient σ_{eff}, results suggest that despite the huge simplifications to pore morphology in the proposed independent scattering solution, good results may be obtained for extremely low porosities ($f_p < 0.05$). However, deviations appear at higher values of f_p due to dependent scattering. In addition, results appear very sensitive to volume element size D, with poor convergence. This is likely due to forward-scattering interference effects [16, 18, 19], which can be seen from the sharp lobes in the scattering phase functions ϕ_{eff} at scattering angles close to 0°. This phenomenon becomes more pronounced with increasing volume element sizes due to the higher number of scattered wavelets, leading to poor convergence behavior.

In radiative transfer theory, as the forward-scattered intensity may simply be treated as unscattered radiation [19, 23], we invoke the transport approximation, which models a material with scattering coefficient σ_{eff} and anisotropic phase function ϕ_{eff} as an isotropically scattering material of transport scattering coefficient σ_{tr} [63]:

$$\sigma_{tr} = \sigma_{\text{eff}}(1 - g_{\text{sca}}) \tag{15}$$

where g_{sca} is the asymmetry parameter defined below:

$$g_{\text{sca}} = \int_{4\pi} \phi_{\text{eff}}(\theta) \cos\theta \, \mathrm{d}\Omega' \tag{16}$$

Figure 16 shows the values of σ_{tr} for all the considered wavelengths obtained on some of the largest volume element sizes. We observe significantly better convergence with increasing volume element size D: results for larger values of D by and large fall within the dispersion observed for smaller values of D. This supports our hypothesis that the poor convergence of σ_{eff} and ϕ_{eff} with respect to D is mainly due to the constructive interference of forward-scattered radiation. It can also be noted that the independent scattering solution for σ_{tr} describes the DDA result fairly well at wavelengths of $\lambda_0 \leq 1.5\,\mu\text{m}$, while at larger wavelengths it still fails beyond $f_p > 0.05$.

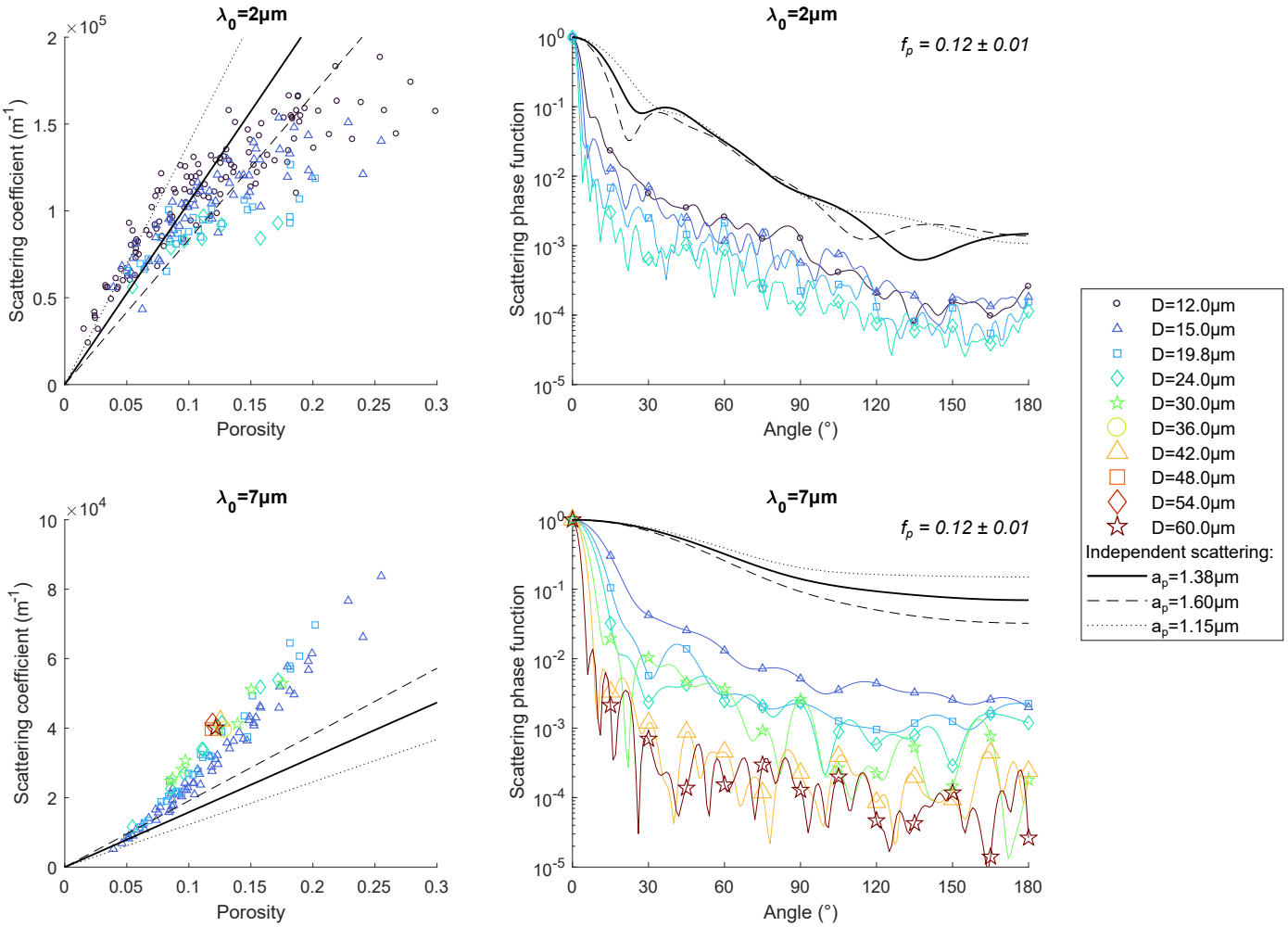

Figure 15: Left: Effective scattering coefficient as a function of porosity computed with the DDA on volume elements of different diameters D (shown as different symbols) for wavelengths $\lambda_0 = 2\,\mu\text{m}$ (top) and $7\,\mu\text{m}$ (bottom). Right: Scattering phase function ϕ_{eff}, averaged over volume elements of porosity $f_p = 0.12 \pm 0.01$ and normalized such that $\phi_{\text{eff}}(0) = 1$, for different volume element sizes. DDA results are compared to the independent scattering model applied to clusters of spherical pores of uniform radii a_p (equation (12)). The influence of a slight variation about the nominal $a_p = 1.38\,\mu\text{m}$ is shown (thick lines vs. dotted lines).

Our results also show that σ_{tr} may be described fairly well at low porosities by the second-order polynomial function below:

$$\sigma_{tr}(f_p, \lambda_0) = p_1(\lambda_0) f_p + p_2(\lambda_0) f_p^2 \tag{17}$$

Values of p_1 and p_2 for the considered wavelengths are given in Table 3. The confidence interval of the proposed correlations, determined from their RMS deviation with respect to the DDA results,

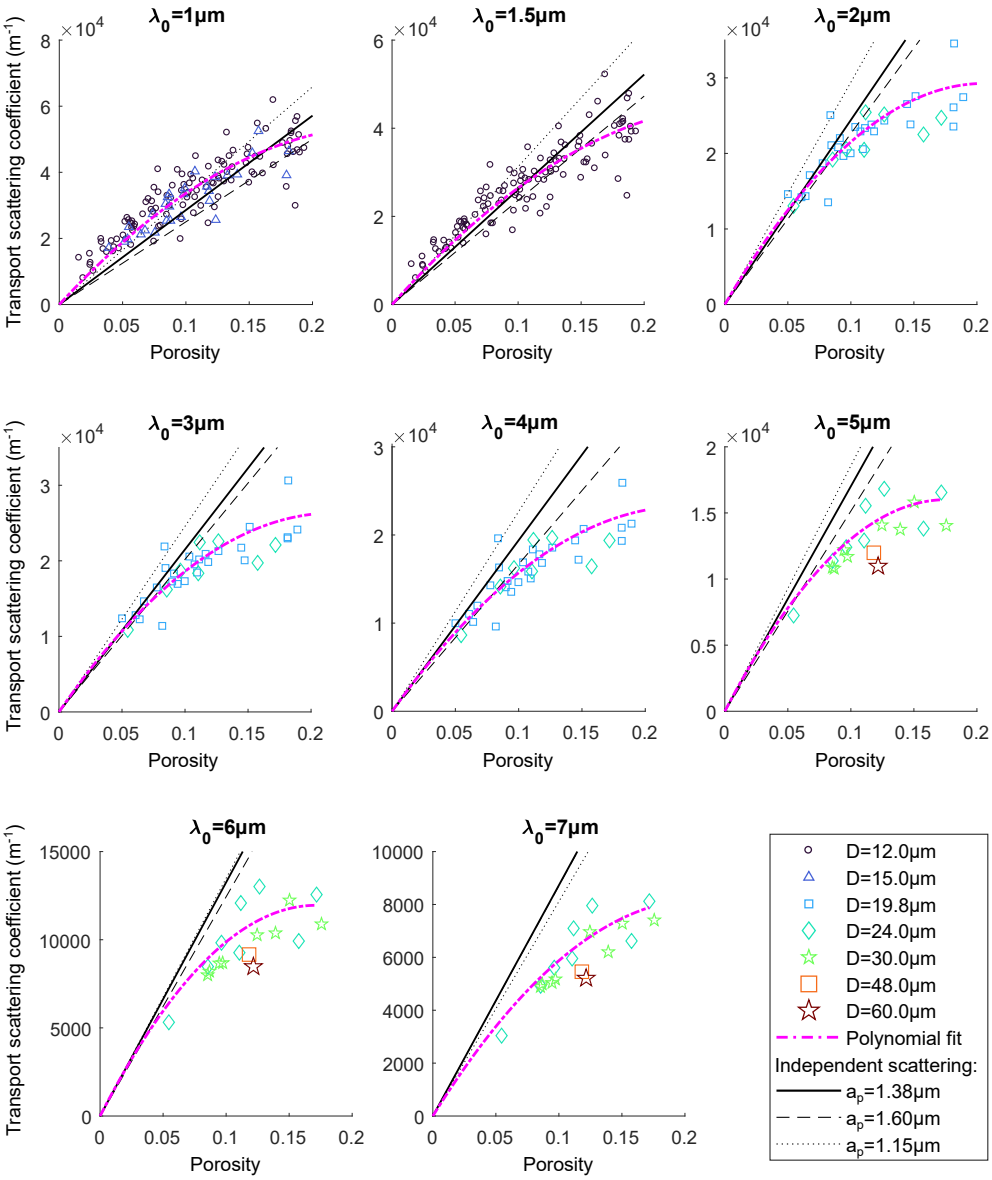

Figure 16: Effective transport scattering coefficient as a function of porosity computed with the DDA on volume elements of different diameters D (shown as different symbols) for wavelengths λ_0 between 1 μm and 7 μm. Converged results are fitted with a second-order polynomial function (thick dash-dotted lines), and compared to the independent scattering model applied to clusters of spherical pores of uniform radii a_p (equation (12)). The influence of a slight variation about the nominal $a_p = 1.38\,\mu\text{m}$ is shown (thick continuous lines vs. thin dotted lines).

reflects the microstructural variability and ranges from 20.8% at $\lambda_0 = 1\,\mu\text{m}$ to 9.8% at $\lambda_0 = 5\,\mu\text{m}$.

4.3. Results of surface reflectivity modeling

We consider the porous alumina surface to be optically smooth everywhere [34] except where pores are present, and modeled it by applying periodic boundary conditions to cuboidal volume

λ_0 (μm)	p_2 (m^{-1})	p_1 (m^{-1})	D (μm)	N	$f_{p,\max}$	RMS deviation (%)
1.0	-7.9752×10^5	4.1620×10^5	12.0	125	0.31	20.8
1.5	-5.6131×10^5	3.2047×10^5	12.0	125	0.31	17.6
2.0	-6.9006×10^5	2.8421×10^5	19.8	27	0.20	12.0
3.0	-5.5285×10^5	2.4132×10^5	19.8	27	0.20	12.1
4.0	-4.3028×10^5	2.0015×10^5	19.8	27	0.20	13.1
5.0	-5.1739×10^5	1.8200×10^5	24.0	8	0.17	9.8
6.0	-4.0644×10^5	1.3940×10^5	24.0	8	0.17	12.5
7.0	-1.7899×10^5	7.6655×10^4	24.0	8	0.17	10.9

Table 3: Coefficients of second-order polynomial correlations describing the transport scattering coefficient σ_{tr} as a function of porosity f_p (see equation 17), extracted from DDA computations on N spherical volume elements of diameter D. The correlations are obtained on the domain $0 < f_p < f_{p,\max}$. The root-mean-squared (RMS) difference between the numerical results and the proposed correlations are also given.

elements of dimensions $h \times L \times L$ sampled at random from the reconstructed material. As the DDA with periodic boundary conditions is computationally much more expensive, fewer volume elements of smaller size were used compared to volume radiative properties modeling. Knowing the extreme sensitivity of directional quantities towards fine microstructural characteristics [39], a large statistical dispersion in numerical results is expected.

Since determination of microstructure-property relations from DDA results would prove tricky given these constraints, we seek instead to compare the DDA results to the predictions of several simpler analytical models. The case of normally incident light with $\lambda_0 = 2\,\mu\text{m}$ is considered. DDA computations are performed with the LDR polarizability and a cell size of $d = 60\,\text{nm}$ corresponding to $y = 0.321$. The substrate parameters are chosen as $h_{\text{sub}} = 4.2\,\mu\text{m}$ and $k_{\text{sub}} = 0.09$ following the method in Appendix A. With these model parameters, the uncertainty in the simulated reflectivity is estimated to be 8.6%. The goal is to use the DDA results to orient the choice of analytical surface reflectivity model.

In Figure 17, DDA results for the normal-normal (ρ_{spec}) and normal-hemispherical (ρ_{h}) reflectivity obtained for volume elements of different dimensions are shown. The symbols ∘, △, and □ represent volume elements of width $L = 5.1\,\mu\text{m}$ and thicknesses $h = 0.9\,\mu\text{m}$, $1.5\,\mu\text{m}$, and $2.1\,\mu\text{m}$ respectively, while ⋄ represent volume elements of $L = 6.3\,\mu\text{m}$ and $h = 1.5\,\mu\text{m}$. Large dispersions are observed in the numerical results, not only due to the high microstructural variability between the small, non-representative volume elements, but also due to wave effects such as resonance

(observed as reflectivity peaks in several of the smaller samples with higher porosity).

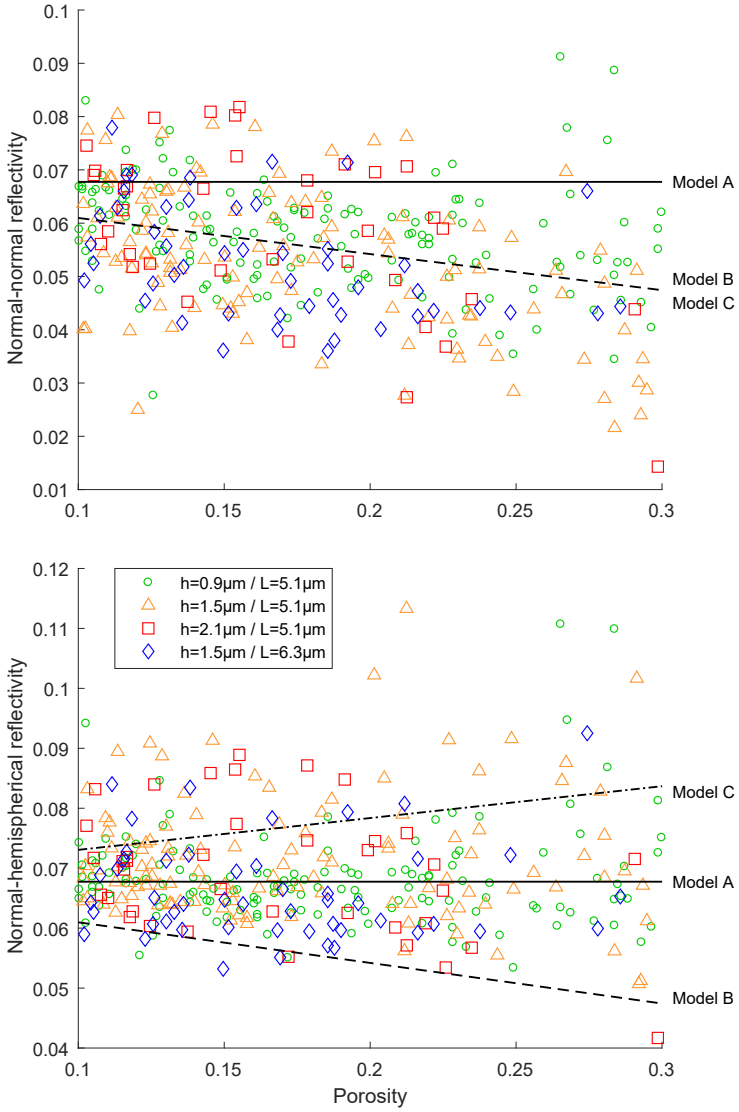

Figure 17: Normal-normal (ρ_{spec}) and normal-hemispherical (ρ_{h}) reflectivity for $\lambda = \lambda_0 = 2\,\mu\mathrm{m}$ as a function of porosity. DDA results obtained on volume elements of various thickness h and width L (symbols) are compared to analytical models based on the geometrical optics approximation (lines).

The three analytical models selected for comparison with DDA results are presented below, with ρ_{Fr} denoting the specular reflectivity obtained from Fresnel's equations [3] using the solid phase complex refractive index ($m_m = n_m + ik_m$):

"Model A" assumes perfectly smooth surfaces that reflect specularly, an assumption commonly

used in past work on radiative transfer in low porosity media [8, 21, 22, 24, 34]:

$$\rho_{\mathrm{h}} = \rho_{\mathrm{spec}} = \rho_{\mathrm{Fr}} \tag{18}$$

"Model B" assumes an infinitesimally thin surface layer, perfectly permeable where pores are present and smooth elsewhere. Reflection is therefore also perfectly specular, and is proportional to the solid phase volume fraction f_m:

$$\rho_{\mathrm{h}} = \rho_{\mathrm{spec}} = f_m \rho_{\mathrm{Fr}} \tag{19}$$

"Model C" assumes a smooth solid surface with pores modeled as locally smooth cavities, which produces diffuse reflection where pores are present on the surface, and specular reflection elsewhere. Diffuse reflection is assumed isotropic and modeled by the incident-cosine-weighted average reflectivity [63, 64]. This gives the following expression for ρ_{h}:

$$\rho_{\mathrm{h}} = \rho_{\mathrm{spec}} + \rho_{\mathrm{diff}} = f_m \rho_{\mathrm{Fr}} + f_p \int_{\hat{\boldsymbol{u}}' \cdot \hat{\boldsymbol{n}} < 0} 2\rho_{\mathrm{Fr}}(\hat{\boldsymbol{u}}') \left| \hat{\boldsymbol{u}}' \cdot \hat{\boldsymbol{n}} \right| \mathrm{d}\Omega' \tag{20}$$

where $\hat{\boldsymbol{n}}$ is the normal vector pointing outwards from the surface.

Despite the large dispersion in numerical results, some clear trends may still be identified. For one, reflection is clearly non-specular with a clear decrease in normal-normal reflectivity (ρ_{spec}) with porosity, which renders Model A inapplicable. On the other hand, for the normal-hemispherical reflectivity (ρ_{h}), between Models B and C, Model C is clearly more appropriate. These observations are supported by the RMS deviations between each model and the DDA results obtained on different volume element sizes, listed in Table 4. Among the three analytical models proposed to model the surface reflectivity, Model C indeed gives the best agreement with the DDA results, with a maximal RMS deviation of 27% on ρ_{spec} and 22.6% on ρ_{h}.

Number of samples		h (μm)	L (μm)	RMS deviation in ρ_{spec} (%) Model A	Models B and C	RMS deviation in ρ_{h} (%) Model A	Model B	Model C
172	∘	0.9	5.1	23.21	19.96	12.07	93.13	17.74
136	△	1.5	5.1	36.04	27.00	18.98	92.75	17.83
99	□	2.1	5.1	31.74	26.16	18.14	93.24	22.61
62	⋄	1.5	6.3	37.71	26.68	14.40	93.51	22.58

Table 4: Root-mean-squared (RMS) deviations between the normal-normal (ρ_{spec}) and normal-hemispherical (ρ_{h}) reflectivity at $\lambda_0 = 2\,\mu\text{m}$ computed with the DDA on volume elements of different thicknesses h and widths L, and predictions of three analytical models based on the geometrical optics approximation.

5. Conclusion

We proposed a numerical approach to predict the effective radiative properties of porous ceramics from physical optics computations on 3D microstructures via the discrete dipole approximation (DDA). Our approach is targeted at porous ceramics composed of a weakly absorbing solid matrix containing low volume fractions of small pores or particles. The tomography-reconstructed microstructure and the complex refractive index of each phase were used as input.

Case studies on reference microstructures were performed to determine the optimal model parameters. We showed that an accuracy of 5% was achieved with the Lattice Dispersion Relation [46] polarizability prescription and a discretization parameter $y < 0.81$ for the volume radiative properties model, and $y < 0.4$ for the surface reflectivity model. We also highlighted the importance of a fine imaging resolution for tomography-reconstructed microstructures due to the strong influence of shape errors.

We then applied our models to compute the volume and surface radiative properties of a tomography-reconstructed porous alumina ceramic with a nominal porosity of 12% and a mean pore size of 1.8 μm. While conventional approaches based on the representative volume element (RVE) are inapplicable, we showed that computations on a large number of small volume elements can provide converged microstructure-property statistics. These were used to validate and/or extract analytical microstructure-property relations for the studied porous alumina. The uncertainty due to microstructural variability was estimated via the root-mean-squared (RMS) deviation between the DDA results and the analytical relations.

Our simulated absorption coefficient κ_{eff} showed good convergence behavior, and confirmed

the applicability of the analytical model by Dombrovsky et al. [12] for the considered wavelengths. On the other hand, the simulated scattering coefficient σ_{eff} and phase function ϕ_{eff} converges poorly with volume element size due to strong forward-scattering interference effects. By considering the transport scattering coefficient $\sigma_{tr} = \sigma_{\text{eff}}(1 - g_{\text{sca}})$ instead, results converge much better with increasing volume element size, and can be described with a second-order polynomial function of the porosity. The independent scattering solution computed from the mean pore chord length agrees well with simulated data for porosities below 5%.

The non-specular surface reflectivity of the porous alumina for 2 µm wavelength radiation at normal incidence was also modeled and used to assess the suitability of several simple analytical models. The model in closest agreement with simulated data considers rays incident on the solid phase to be reflected specularly according to Fresnel's equations, and rays incident on the pore phase to be diffusely reflected with the reflectivity given by Siegel and Spuckler [64].

In the next part of our study presented in our companion paper [41], the determined radiative properties are applied to radiative transfer simulations of the reflectance, transmittance and emittance of thin porous alumina samples. Comparison with spectroscopic measurements allows us to validate the numerical methodology notably the physical optics approach proposed in this work. The validated approach would be of great interest to future work on microstructure-based prediction of the radiative behavior of high-performance porous ceramics.

6. Acknowledgments

This research was supported by Saint-Gobain Research (SGR) Provence and the French National Association for Research and Technology (ANRT) through the CIFRE grant number 2017/0775. The authors would like to express their gratitude to L. San Miguel (SGR Provence), L. Pierrot (SGR Provence) and J. Meulemans (SGR Paris) for their insight and discussions that greatly improved the research; to Y. Millot (SGR Provence) for sample preparation; to J. Adrien (MATEIS) and N. Naouar (LaMCoS) for assistance with X-ray tomography; and to D. De Sousa Meneses (CEMHTI) for provision of optical data and helpful discussions. Special thanks also go to authors who graciously made their codes available on the public domain: B.T. Draine and P.

Flatau (DDSCAT), J. Schäfer (MatScat), S.J. Byrnes (TMM), and M.R. MacIver (chord length calculator).

Appendix A. Non-reflecting boundary conditions on semi-infinite layers using an absorbing substrate

The bidirectional surface reflectivity model proposed in section 2.2.3 considers reflection from a semi-infinite layer of the heterogeneous material (with a dominant matrix phase of complex refractive index $m_m = n_m + ik_m$) illuminated from the top. Non-reflecting boundary conditions are applied to the bottom surface by the addition of an absorbing substrate of thickness h_{sub} and refractive index $m_{\text{sub}} = n_{\text{sub}} + ik_{\text{sub}}$. This appendix explains how the amount of light reflected off the boundary between the top layer and the substrate depends on the substrate properties, and how an appropriate choice of said properties can be made to minimize this reflection.

Interface reflection [3], labeled as ① in Figure A.18a, occurs due to the mismatch in refractive indexes on both sides of the interface. To minimize the mismatch between the top layer and the substrate, we set $n_{\text{sub}} = n_m$ and limit the absorption index k_{sub} of the substrate to small values (less than 0.1).

Some of the light entering the substrate may experience one or multiple reflections off the bottom surface of the substrate in contact with the ambient medium before traveling back to the top layer. This source of reflection is labeled as ② in Figure A.18a. For a given k_{sub}, the substrate thickness h_{sub} should thus be as large as possible to maximize absorption, with memory constraints limiting the number of dipoles and thus the thickness that can be simulated.

This undesired reflection at the boundary between the top layer and the substrate may be estimated from the reflectance of a semi-infinite substrate of refractive index m_{sub} and thickness h_{sub}, placed between an infinite upper layer of refractive index m_m and an infinite bottom layer of refractive index n_{amb} and illuminated from above (same configuration as in Figure A.18a). Analytical solvers of Maxwell's equations for multi-layered systems, such as the Python "Transfer Matrix Method" package [57], can be used to simulate such a configuration. Figure A.18b plots the normal boundary reflectivity at $\lambda_0 = 1\,\mu\text{m}$ as a function of absorption index k_{sub} for three different substrate thicknesses h_{sub}, with $n_m = 1.718 = n_{\text{sub}}$, $k_m = 0$ and $n_{\text{amb}} = 1$. For a given thickness,

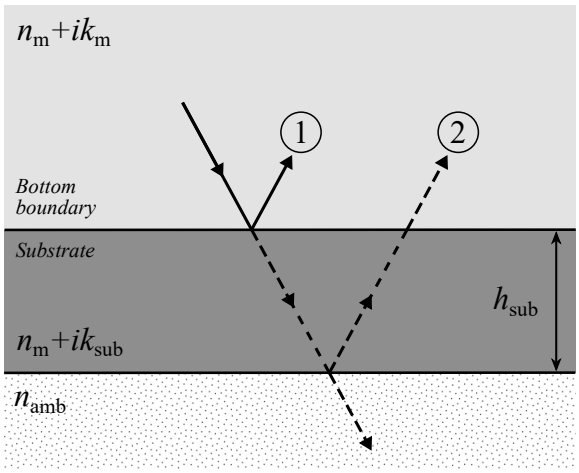

(a) Reflection at the bottom boundary.

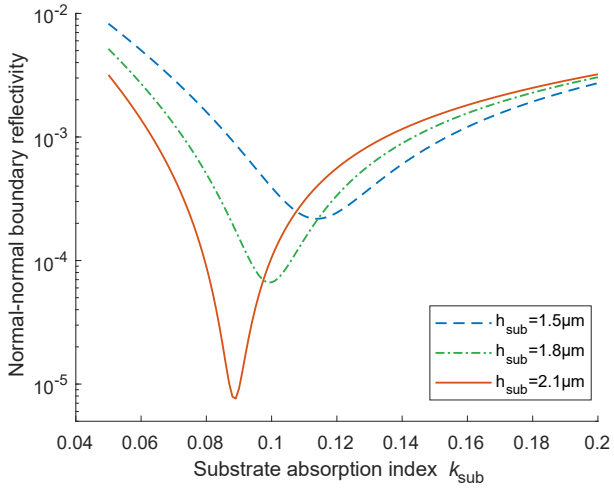

(b) Boundary reflectivity for different substrate parameters.

Figure A.18: Simulation of non-reflecting boundary conditions by the addition of an absorbing substrate: the substrate properties determine the amount of reflection at the boundary between the top layer and the substrate.

we see that the boundary reflectivity initially decreases with increasing absorption index as the reflection from source ② diminishes, but then reaches a minimum and increases as the reflection from source ① becomes more significant. Furthermore, the results suggest that there exists a single combination of k_{sub} and h_{sub} that minimizes the boundary reflectivity, which corresponds to $k_{sub} = 0.09$ and $h_{sub} = 2.1$ μm among the investigated combinations.

A limitation to this method lies in the fact that the optimal combination of substrate parameters varies with incidence angle. In simulations involving heterogeneous materials, light arrives at the bottom surface of the top layer at a wide range of incidence angles that is difficult to know

beforehand. Simplifying assumptions (e.g., near-normal incidence) are therefore required when choosing the substrate parameters.

References

[1] R. Viskanta, M. P. Mengüç, Radiative Transfer in Dispersed Media, Applied Mechanics Reviews 42 (1989) 241–259.

[2] L. Dombrovsky, D. Baillis, Thermal Radiation in Disperse Systems: An Engineering Approach, Begell House, 2010.

[3] J. Howell, M. Menguc, R. Siegel, Thermal Radiation Heat Transfer, 6th Edition, 6 ed., Taylor & Francis, 2015.

[4] A. Kaemmerlen, C. Vo, F. Asllanaj, G. Jeandel, D. Baillis, Radiative properties of extruded polystyrene foams: Predictive model and experimental results, Journal of Quantitative Spectroscopy and Radiative Transfer 111 (2010) 865–877.

[5] J. Randrianalisoa, W. Lipiński, Effect of pore-level geometry on far-field radiative properties of three-dimensionally ordered macroporous ceria particle, Applied Optics 53 (2014) 1290.

[6] Y. Li, H. W. Chen, X. L. Xia, G. Y. Ma, H. P. Tan, Prediction of high-temperature radiative properties of copper, nickel, zirconia, and alumina foams, International Journal of Heat and Mass Transfer 148 (2020) 119154.

[7] X. Chen, C. Zhao, B. Wang, Microstructural effect on radiative scattering coefficient and asymmetry factor of anisotropic thermal barrier coatings, Journal of Quantitative Spectroscopy and Radiative Transfer 210 (2018) 116 – 126.

[8] B. Bouvry, L. Del Campo, D. De Sousa Meneses, O. Rozenbaum, R. Echegut, D. Lechevalier, M. Gaubil, P. Echegut, Hybrid Methodology for Retrieving Thermal Radiative Properties of Semi-Transparent Ceramics, Journal of Physical Chemistry C 120 (2016) 3267–3274.

[9] B. Zeghondy, E. Iacona, J. Taine, Experimental and RDFI calculated radiative properties of a mullite foam, International Journal of Heat and Mass Transfer 49 (2006) 3702–3707.

[10] Y. Li, X.-L. Xia, C. Sun, S.-D. Zhang, H.-P. Tan, Volumetric radiative properties of irregular open-cell foams made from semitransparent absorbing-scattering media, Journal of Quantitative Spectroscopy and Radiative Transfer 224 (2019) 325–342.

[11] S. Lallich, F. Enguehard, D. Baillis, Experimental Determination and Modeling of the Radiative Properties of Silica Nanoporous Matrices, Journal of Heat Transfer 131 (2009) 082701.

[12] L. Dombrovsky, J. Randrianalisoa, D. Baillis, L. Pilon, Use of Mie theory to analyze experimental data to identify infrared properties of fused quartz containing bubbles, Applied optics 44 (2005) 7021–7031.

[13] J. Randrianalisoa, D. Baillis, L. Pilon, Modeling radiation characteristics of semitransparent media containing bubbles or particles, J. Opt. Soc. Am. A 23 (2006) 1645–1656.

[14] C. F. Bohren, D. R. Huffman, Absorption and Scattering of Light by Small Particles, John Wiley & Sons, Inc., 1983. doi:10.1002/9783527618156.

[15] Z. Ivezic, M. P. Menguc, An investigation of dependent / independent scattering regimes using a discrete dipole approximation, International Journal of Heat and Mass Transfer 39 (1996) 811–822.

[16] M. I. Mishchenko, L. Liu, D. W. Mackowski, B. Cairns, G. Videen, Multiple scattering by random particulate media: exact 3d results, Opt. Express 15 (2007) 2822–2836.

[17] M. I. Mishchenko, L. Liu, G. Videen, Conditions of applicability of the single-scattering approximation, Opt. Express 15 (2007) 7522–7527.

[18] M. I. Mishchenko, "independent" and "dependent" scattering by particles in a multi-particle group, OSA Continuum 1 (2018) 243–260.

[19] B. Wang, C. Zhao, Effect of dependent scattering on light absorption in highly scattering random media, International Journal of Heat and Mass Transfer 125 (2018) 1069 – 1078.

[20] T. Galy, D. Huang, L. Pilon, Journal of Quantitative Spectroscopy & Radiative Transfer Revisiting independent versus dependent scattering regimes in suspensions or aggregates of spherical particles, Journal of Quantitative Spectroscopy and Radiative Transfer 246 (2020) 106924.

[21] B. Rousseau, D. De Sousa Meneses, P. Echegut, M. Di Michiel, J. F. Thovert, Prediction of the thermal radiative properties of an x-ray μ-tomographied porous silica glass, Applied Optics 46 (2007) 4266–4276.

[22] B. Rousseau, J.-y. Y. Rolland, P. Echegut, L. Del Campo, D. De Sousa Meneses, P. Echegut, Modelling of the Thermal Radiative Properties of Oxide Ceramics, in: Proceedings of the 14th International Heat Transfer Conference, 13, 2010, pp. 1–6.

[23] J. Randrianalisoa, D. Baillis, Radiative properties of densely packed spheres in semitransparent media: A new geometric optics approach, Journal of Quantitative Spectroscopy and Radiative Transfer 111 (2010) 1372 – 1388.

[24] O. Rozenbaum, C. Blanchard, D. De Sousa Meneses, Determination of high-temperature radiative properties of porous silica by combined image analysis, infrared spectroscopy and numerical simulation, International Journal of Thermal Sciences 137 (2019) 552–559.

[25] M. Kahnert, Numerical solutions of the macroscopic Maxwell equations for scattering by non-spherical particles: A tutorial review, Journal of Quantitative Spectroscopy and Radiative Transfer 178 (2016) 22–37.

[26] E. M. Purcell, C. R. Pennypacker, Scattering and Absorption of Light by Nonspherical Dielectric Grains, The Astrophysical Journal 186 (1973) 705.

[27] B. T. Draine, P. J. Flatau, Discrete-Dipole Approximation For Scattering Calculations, Journal of the Optical Society of America A 11 (1994) 1491.

[28] B. T. Draine, P. J. Flatau, Discrete-dipole approximation for periodic targets: theory and tests, Journal of the Optical Society of America A 25 (2008) 2693.

[29] M. A. Yurkin, M. Min, A. G. Hoekstra, Application of the discrete dipole approximation to very large refractive indices: Filtered coupled dipoles revived, Physical Review E 82 (2010) 036703.

[30] V. M. Wheeler, J. Randrianalisoa, K. Tamma, W. Lipiński, Spectral radiative properties of three-dimensionally ordered macroporous ceria particles, Journal of Quantitative Spectroscopy and Radiative Transfer 143 (2014) 63–72.

[31] X. Dai, S. Haussener, Optical characterization of multi-scale morphologically complex heterogeneous media – application to snow with soot impurities, Journal of Quantitative Spectroscopy and Radiative Transfer 206 (2018) 378 – 391.

[32] Y. Bao, Y. Huang, W. Li, K. Zhu, Combination of the monte carlo method and dda to evaluate the radiative properties of ito- pigmented and tio2-pigmented coatings, International Journal of Thermal Sciences 146 (2019) 106076.

[33] R. Coquard, D. Baillis, D. Quenard, Energy & Buildings Numerical and experimental study of the IR opacification of polystyrene foams for thermal insulation enhancement, Energy & Buildings 183 (2019) 54–63.

[34] S. Guévelou, B. Rousseau, G. Domingues, J. Vicente, A simple expression for the normal spectral emittance of open-cell foams composed of optically thick and smooth struts, Journal of Quantitative Spectroscopy and Radiative Transfer 189 (2017) 329 – 338.

[35] P. Beckmann, A. Spizzichino, The Scattering of Electromagnetic Waves from Rough Surfaces, Pergamon Press Ltd., 1963.

[36] K. Tang, R. A. Dimenna, R. O. Buckius, Regions of validity of the geometric optics approximation for angular scattering from very rough surfaces, International Journal of Heat and Mass Transfer 40 (1996) 49 – 59.

[37] J. Elson, H. Bennett, J. Bennett, Chapter 7 - scattering from optical surfaces, volume 7 of *Applied Optics and Optical Engineering*, Elsevier, 1979, pp. 191 – 244. URL: http://www.sciencedirect.com/science/article/pii/B9780124086074500141. doi:https://doi.org/10.1016/B978-0-12-408607-4.50014-1.

[38] H. Ragheb, E. R. Hancock, Testing new variants of the beckmann–kirchhoff model against radiance data, Computer Vision and Image Understanding 102 (2006) 145 – 168.

[39] B. Liu, X. Xia, X. Zhang, C. Sun, Spectral radiative properties of skeleton inner structure of ceramic foam based on ordered opal structure model, Journal of Quantitative Spectroscopy and Radiative Transfer 224 (2019) 279 – 288.

[40] B. Liu, X.-l. Xia, C. Sun, X. Chen, Analysis on spectral radiative properties of micro-scaled rough ligament surface inside open-cell nickel foam, International Journal of Heat and Mass Transfer 145 (2019) 118773.

[41] Z. Low, A. Novikov, D. De Sousa Meneses, D. Baillis, 2– radiative behavior of porous alumina up to high temperatures: Experiments and physical optics-based modeling, 2020. In preparation.

[42] W. Lipiński, J. Petrasch, S. Haussener, Application of the spatial averaging theorem to radiative heat transfer in

two-phase media, Journal of Quantitative Spectroscopy and Radiative Transfer 111 (2010) 253–258.

[43] B. T. Draine, The discrete-dipole approximation and its application to interstellar graphite grains, The Astrophysical Journal 333 (1988) 848.

[44] M. Yurkin, A. Hoekstra, The discrete dipole approximation: An overview and recent developments, Journal of Quantitative Spectroscopy and Radiative Transfer 106 (2007) 558 – 589. IX Conference on Electromagnetic and Light Scattering by Non-Spherical Particles.

[45] M. A. Yurkin, V. P. Maltsev, A. G. Hoekstra, Convergence of the discrete dipole approximation. I. Theoretical analysis, Journal of the Optical Society of America A 23 (2006) 2578.

[46] D. Gutkowicz-Krusin, B. T. Draine, Propagation of Electromagnetic Waves on a Rectangular Lattice of Polarizable Points (2004) 1–17.

[47] B. T. Draine, P. J. Flatau, User Guide for the Discrete Dipole Approximation Code DDSCAT 7.3, 2019.

[48] R. D. da Cunha, T. Hopkins, The Parallel Iterative Methods (PIM) package for the solution of systems of linear equations on parallel computers, Applied Numerical Mathematics 19 (1995) 33–50.

[49] M. Petravic, G. Kuo-Petravic, ILUCG algorithm which minimizes in the Euclidean norm, Technical Report July, Princeton Plasma Physics Laboratory (PPPL), Princeton, NJ (United States), 1978. URL: http://www.osti.gov/servlets/purl/6611598-bsiTOx/. doi:10.2172/6611598.

[50] R. Coquard, D. Baillis, Radiative Characteristics of Beds of Spheres Containing an Absorbing and Scattering Medium., Journal of Thermophysics and Heat Transfer 19 (2005) 226–234.

[51] Y. Li, X. L. Xia, C. Sun, Q. Ai, B. Liu, H. P. Tan, Tomography-based analysis of apparent directional spectral emissivity of high-porosity nickel foams, International Journal of Heat and Mass Transfer 118 (2018) 402–415.

[52] T. Kanit, S. Forest, I. Galliet, V. Mounoury, D. Jeulin, Determination of the size of the representative volume element for random composites: Statistical and numerical approach, International Journal of Solids and Structures 40 (2003) 3647–3679.

[53] Z. Low, N. Blal, N. Naouar, D. Baillis, Influence of boundary conditions on computation of the effective thermal conductivity of foams, International Journal of Heat and Mass Transfer 155 (2020) 119781.

[54] N. B. Piller, O. J. Martin, Increasing the performance of the coupled-dipole approximation: A spectral approach, IEEE Transactions on Antennas and Propagation 46 (1998) 1126–1137.

[55] J.-P. Schäfer, Implementierung und Anwendung analytischer und numerischer Verfahren zur Lösung der Maxwellgleichungen für die Untersuchung der Lichtausbreitung in biologischem Gewebe, Doctoral thesis, Universität Ulm, 2011. doi:10.18725/OPARU-1914.

[56] M. R. MacIver, M. Pawlik, Analysis of in situ microscopy images of flocculated sediment volumes, Chemical Engineering & Technology 40 (2017) 2305–2313.

[57] S. J. Byrnes, Multilayer optical calculations (2016) 1–20.

[58] D. C. Harris, L. F. Johnson, L. Cambrea, L. Baldwin, M. Baronowski, E. Zelmon, W. B. Poston, J. D. Kunkel,

M. Parish, M. R. Pascucci, J. J. Gannon, Jr, T.-c. Wen, Refractive index of infrared- transparent polycrystalline alumina, Optical Engineering 56 (2017) 077103.

[59] L. A. Pajdzik, A. M. Glazer, Three-dimensional birefringence imaging with a microscope tilting-stage. I. Uniaxial crystals, Journal of Applied Crystallography 39 (2006) 326–337.

[60] J. F. Brun, L. del Campo, D. De Sousa Meneses, P. Echegut, Infrared optical properties of alpha-alumina with the approach to melting: gamma-like tetrahedral structure and small polaron conduction, Journal of Applied Physics 114 (2013) 223501.

[61] J. Schindelin, I. Arganda-Carreras, E. Frise, V. Kaynig, M. Longair, T. Pietzsch, S. Preibisch, C. Rueden, S. Saalfeld, B. Schmid, J.-Y. Tinevez, D. J. White, V. Hartenstein, K. Eliceiri, P. Tomancak, A. Cardona, Fiji: an open-source platform for biological-image analysis, Nature Methods 9 (2012) 676–682.

[62] W. de Kruijf, J. Kloosterman, On the average chord length in reactor physics, Annals of Nuclear Energy 30 (2003) 549–553.

[63] L. A. Dombrovsky, The use of transport approximation and diffusion-based models in radiative transfer calculations, Computational Thermal Sciences: An International Journal 4 (2012) 297–315.

[64] R. Siegel, C. Spuckler, Approximate solution methods for spectral radiative transfer in high refractive index layers, International Journal of Heat and Mass Transfer 37 (1994) 403 – 413.